

https://dspace.org/

The study of amorphous gallium arsenide (GaAs)

Mpatani, Ongeziwe

2022
https://hdl.handle.net/10539/34485

Downloaded from a DSpace repository. https://dspace.org/

The Study of Amorphous Gallium Arsenide (GaAs)

Ongeziwe Mpatani

A dissertation submitted to the Faculty of Science, University of the Witwatersrand, Johannesburg in fulfilment of the academic requirements for the degree of Master of Science

June 14, 2022

Declaration

I declare that this dissertation is my own, unaided work. It is being submitted for the Degree of Master of Science at the University of the Witwatersrand, Johannesburg. It has not been submitted before for any degree or examination at any other University.



Signature:.....

Date: 14/06/2022

Abstract

GaAs is a widely used semiconductor material when doped with different elements of the periodic table to enhance its properties. Over the years, doping has been well established by ion implantation where the induced defects and/or amorphization influences the desired properties for practical applications. In the present investigation, implantations using argon and silicon ions were carried out on crystalline GaAs (c-GaAs) to create a near-surface amorphous layer (a-GaAs). The project aimed to demonstrate how different energies and doses of implantation affect both the damage profile and thickness of the amorphous layer and in turn determine the elastic constants of c-GaAs and a-GaAs.

Surface Brillouin scattering (SBS) was used to determine these elastic constants. SBS is an optical technique that probes the nature of surface acoustic excitations propagating on thin films, multilayered and bulk materials. In opaque materials, such as GaAs, the surface ripple mechanism governs the inelastic scattering of light. The measured frequency of the inelastically scattered light is equal to the frequency of the phonon created or annihilated during scattering. This, combined with momentum conservation determines the phonon wave vector. Additionally, for a specific scattering geometry, this data gives the acoustic velocity of the propagating modes and through the inverse problem approach that is used to estimate the elastic constants of the material.

Raman spectroscopy was employed to study materials crystallinity with implantation induced disorder because the Raman line is sensitive to the crystal structure and its changes. Due to this characteristic, the level of amorphization as a result of both energy and dose was traced. This analysis method is mediated by the Raman effect which explains the inelastic interaction of matter with light.

Several complimentary techniques were utilized to study how the different implantation conditions affect the physical properties of GaAs. These experimental methods include; X-ray diffraction (XRD), grazing incidence X-ray diffraction (GIXRD) and X-ray reflectivity (XRR). Information such as the density of the un-implanted and implanted samples coupled with the crystallite sizes of the implanted samples were determined.

Dedication

To My Mother and Family

Acknowledgement

I am sincerely thankful to my supervisors Prof D.M Wamwangi, Dr K Jakata and Dr H Masenda for their guidance and support throughout the project. I am deeply grateful to them for their encouragement and sharing of knowledge. It is their belief in me and my potential that has made me the researcher I am today. I wish to thank Mr A Miller from iThemba labs for helping with ion implantation of my samples. I am genuinely appreciative of the help from Dr R.M Erasmus for the Raman spectroscopy measurements and analysis and Mr A Shnier for his assistance with the X-ray measurements. To my fellow colleagues in the post graduate PM offices thank you. A special thank you goes to Ms M Baloi and Mr G Mwenda for your kind nature and always being available to assist me. I am grateful to the Council of Scientific and Industrial Research (CSIR) for their financial and psycho-social support. Lastly, I wish to thank my mother for supporting me during the most challenging and most rewarding times of this Masters research. I wish to also thank my family and friends for their support and encouragement.

Contents

1 Introduction **1**

1.1 Literature review 2

1.2 Problem statement 4

1.3 Aims and objectives of this study 5

1.4 Outline of the dissertation 5

2 Surface Brillouin scattering (SBS) **6**

2.1 Theory of surface Brillouin scattering 6

2.1.1 Elastic constants 7

2.1.2 Elastic wave propagation in isotropic solids 9

2.1.3 Scattering mechanism 11

2.1.4 Surface elastodynamics Green's function 12

3 Material modification and experimental details **16**

3.1 Ion implantation 16

3.1.1 Principles of ion implantation 17

3.1.2 Ion implantation parameters and simulations 18

3.2 SBS experimental details 20

3.3 Raman spectroscopy 24
3.3.1 Principles of Raman spectroscopy 25
3.3.2 Raman spectroscopy experimental details 27
3.4 X-ray Diffraction (XRD) and grazing incidence X-ray diffraction (GIXRD) 29
3.5 X-ray reflectivity (XRR) 31

4 Results and Discussion **35**

4.1 Raman spectroscopy 35
4.1.1 Argon implanted GaAs 36
4.1.2 Silicon implanted GaAs 39
4.2 X-ray diffraction (XRD) and grazing incidence X-ray diffraction (GIXRD) 42
4.3 X-ray reflectivity (XRR) 45
4.4 Surface Brillouin scattering (SBS) 47
4.4.1 Determining the elastic constants of single crystal GaAs 48
4.4.2 Ion implanted GaAs 51
4.4.3 Determination of elastic constant for ion implanted GaAs 56

5 Summary and conclusion **62**

List of Figures

2.1 The wave vectors describing the interaction of the laser with a material. 11

2.2 The scattering geometry of an SBS experiment. 12

2.3 A simulation of the c-GaAs spectrum produced by the surface elastodynamics Green's function. This simulation was performed using literature values:[1] elastic constants $C_{11} = 120$, $C_{12} = 57.6$ and $C_{44} = 58$ GPa and density $\rho = 5.34$ g/cm^3 at incident angle of 71° 14

2.4 A typical measured SBS spectrum of c-GaAs showing the Stokes and anti-Stokes doublet. The peak at 0 GHz corresponds to elastic scattering obtained using the reference light source. 15

3.1 SRIM simulations of the depth profiles of GaAs implanted with $^{40}Ar^{+}$ and $^{30}Si^{+}$ with energies ranging from 30 - 150 keV. 19

3.2 The external SBS experimental set-up showing the path travelled by the beam to the interferometer. 21

3.3 The 3-axis translation stage with azimuthal and scattering angle rotation. 22

3.4 The geometry of the tandem interferometer. 23

3.5 Energy diagram showing transitions for a) Rayleigh scattering, b) Stokes scattering and c) anti-Stokes scattering. 25

3.6 A Raman spectrum with Stokes, Rayleigh and anti-Stokes scattering lines. 26

3.7 A schematic diagram of the Raman scattering experimental set-up. 28

3.8 A schematic of X-rays incident on a crystal lattice where the black circles represent the atoms and the lines the imaginary planes. 30

3.9 A schematic of the scattering that occurs in an XRR experiment. 32

3.10 A typical XRR spectra with details on how the XRR parameters can be established. 33

3.11 An XRR spectra of GaAs before, *c*-GaAs, and after ion implantation, *a*-GaAs: Ar^+ 1×10^{16} ions/cm^2. 34

4.1 A Raman spectrum of *c*-GaAs with a simulated fit (red). The spectrum has an LO phonon peak (blue) at 291.24 cm^{-1} and a TO phonon peak (green) at 268.18 cm^{-1}. 36

4.2 The Raman spectra of argon implanted GaAs where a) shows the spectra of the samples implanted with different ion doses while b) shows the spectra of the samples implanted with varying energies. 37

4.3 The FWHM and Raman position for argon implanted GaAs where a) shows the parameters as a function of dose and b) of energy. 38

4.4 The Raman spectra of silicon implanted GaAs, where a) shows the spectra of the samples implanted with different ion doses and b) shows the spectra of the samples implanted with varying ion energies. 40

4.5 The FWHM and Raman position for silicon implanted GaAs where a) shows the parameters as a function of dose and b) of energy. 41

4.6 An XRD pattern of pristine GaAs. 42

4.7 A GIXRD pattern of GaAs following implantation with a) argon and b) silicon ions of the lowest, second highest and highest dose taken at grazing incidence of $\omega_i = 1°$. 44

4.8 An example of the fit performed to establish the density of the un-implanted GaAs sample using LEPTOS. 46

4.9 The dispersion curve of the Rayleigh SAW mode of *c*-GaAs which was used to identify the [100] and [110] propagation directions. 49

4.10 The Lamb shoulder region of the anti-Stokes side of SBS measurement taken in the [100] direction. 50

4.11 An SBS spectrum of a-GaAs. 51

4.12 The dispersion curve of a-GaAs showing its isotropic surface. 52

4.13 A series of SBS spectra of a-GaAs after argon ion implantation at varying doses measured at an incident angle of $\theta = 70°$. 53

4.14 The SBS spectra of a-GaAs after argon ion implantation at different energies measured at an incident angle of $\theta = 70°$. 53

4.15 The anti-Stokes SBS spectra of a-GaAs after silicon ion implantation with different doses measured at an incident angle of $\theta = 70°$. 55

4.16 The anti-Stokes SBS spectra of a-GaAs following silicon ion implantation with varying energies measured at an incident angle of $\theta = 70°$. 56

4.17 The velocity dispersion curve of the a-GaAs samples that were implanted with argon ions of energies from 30 – 150 keV. 57

4.18 The velocity dispersion curve for the a-GaAs samples that were implanted with silicon ions of energies from 30 – 150 keV. 58

4.19 The contour plot of a-GaAs formed from implantation with Ar^+ obtained after an optimized minimization of χ^2 to find the elastic constants and their uncertainties. . . 59

4.20 The contour plot of a-GaAs formed from implantation with Si^+ obtained after an optimized minimization of χ^2 to find the elastic constants and their uncertainties. . . 60

List of Tables

2.1 The phase velocity equations for cubic symmetry materials[2] 9

3.1 The ion implantation conditions used on (001) GaAs. 18

3.2 Tabulated SRIM thicknesses obtained from the two figures above. 20

4.1 The crystallite sizes as determined by the Scherrer equation. 45

4.2 The densities of *a*-GaAs as determined by XRR. 47

4.3 The measured frequencies in the [100] and [110] direction and their corresponding velocities extracted from the dispersion curve of *c*-GaAs. 49

4.4 The elastic constants of *c*-GaAs as obtained from various methods. 50

Chapter 1

Introduction

Gallium arsenide (GaAs) is a III-V compound semiconductor with a zinc-blende structure. It comprises face-centred cubic (fcc) translational symmetry and a two atom basis, with a ^{31}Ga atom at (0,0,0) and a ^{33}As atom at (1/4,1/4,1/4). For this symmetry, each Ga atom is four fold coordinated to As through covalent bonds. GaAs has a density of 5.32 g/cm^3 and direct bandgap energy of 1.42 eV at room temperature[3,4].

GaAs has superior physical properties that often make it better than silicon; giving it numerous advantages in device applications. It has extraordinary electronic and optical properties such as high electron mobility, direct bandgap, and exceptional heat resistance. GaAs and other III-V semiconductors have higher conduction electron velocity compared to silicon because of their smaller effective mass. This makes it suitable for high frequency electronic applications. Additionally, this material is an ideal candidate for optoelectronic devices since its free electrons can easily recombine with holes to efficiently emit light[4–6].

Moreover, semi-insulating GaAs permits a reduction in parasitic capacitance when used as substrates. This characteristic combined with high electron mobility and high-frequency operations leads to higher signal amplification and faster switching speeds. These attributes have made it useful in microwave integrated circuits (ICs), light-emitting diodes (LEDs) and solar cell devices. These devices usually operate with n-type (and p-type) films[5,7].

Ion implantation is the preferred technique for the modification of the physical properties of solids, especially semiconductors because of the ability to control the numbers of atoms and their depth profile. On the other hand, it often induces intentional or unintended damage in crystalline materials through the formation of defects and/or an amorphous layer that affects the elastic and opto-elastic properties of semiconductors. The nature of the damage is determined by the ion energy, ion

dose and dose rate and ion current[8,9]. This research seeks to explore the changes in the physical and structural properties induced by ion implantation on (001) GaAs and determine the elastic properties of its amorphous counterpart using surface Brillouin scattering. Properties of a material such as the elastic constants are important for the optimization of GaAs-based multilayer devices for optoelectronic applications.

1.1 Literature review

Surface Brillouin scattering (SBS) is a non-destructive technique used to determine the elastic properties of thin films, multilayered systems and superlattices. This is achieved through the measurement of the frequency shifts from laser light inelastically scattered by thermally excited acoustic phonons. Léon Brillouin[10] pioneered research on the interaction of light and thermally excited acoustic phonons and Leonid Mandelshtam[11] followed shortly after. The development of lasers enabled experiments that confirmed that SBS was an excellent technique for determining the elastic and photo-elastic properties of materials. The invention of high-contrast spectrometers facilitated the measurement of small and opaque materials as well. Before then the technique was restricted to bulk modes of transparent materials at ambient and elevated temperatures[12,13].

Opaque materials have surface phonons with small amplitudes moving in thermal equilibrium creating ripples that diffract light. As a result, there is little to no transmission of scattered light. This leads to scattering being restricted to the surface of the material making the ripple mechanism dominant over the elasto-optic scattering mechanism. The latter is observed in transparent solids where transmitted light is scattered by phonons in the bulk material. In multilayered systems, the variations of elastic properties and the mass density of the layer(s) and the substrate determines the type of excitations that are observed. TiN (titanium nitride) on high speed-steel is an example of a fast on slow combination. This system is defined by the transverse bulk wave velocity of the layer being greater than that of the substrate. TiN, in this case, is elastically harder than the high speed-steel substrate[14,15]. In such a system surface acoustic wave (SAW), pseudo-SAW, pre-Rayleigh and quasi-Rayleigh are some of the excitations observed. SBS measurements performed on TiN film have shown the propagation of only the SAW and Lamb shoulder as the only modes present for small thicknesses. As the thickness increases the pseudo-SAW comes about and upon further increase, the pre-Rayleigh mode develops. Thereafter the quasi-Rayleigh with higher-order modes. The pre-Rayleigh appears when the shear velocity of the film exceeds that of the substrate. Conversely, TaN (tantalum nitride) on Si thin films make a slow on fast combination where the Rayleigh SAW and Sezawa waves are the excitations observed[16]. A slow on fast system is one in

which the transverse bulk-wave velocity of the layer is less than that of the substrate. The frequency shift of the Rayleigh SAW decreases while the Sezawa wave peaks increase in number and get closer together as the thickness of the film increases. This form of dispersion illustrates acoustic softening with increasing film thicknesses. Another example of a slow on fast system is that of *a*-GaAs on a *c*-GaAs substrate. This is due to *a*-GaAs being elastically softer than *c*-GaAs.

There are a few reports on the comprehensive studies of the physical properties of *a*-GaAs[8,17,18]. The limited literature revealed that the SBS spectrum of *a*-GaAs differs from its crystalline counterpart (*c*-GaAs). When argon ions are implanted into GaAs at a dose of 5×10^{16} ions/cm^2 and energy of 100 keV, an amorphous layer of GaAs is created in the damaged region[8]. This was evident with the presence of the Sezawa wave peak, a mode that was not observed for the anisotropic sample. Another indicator of the amorphous layer was the acoustic softening of the Rayleigh SAW mode (reduced frequency shift). This decrease was also observed for GaAs implanted with tellurium ions at a dose of 1×10^{15} ions/cm^2 and energy 250 keV at low temperature and low current[17]. Furthermore, it was also reported by Ref.[18] when GaAs was implanted with krypton ions of 1.5 MeV energy and doses in the range of 2×10^{13} - 8×10^{14} ions/cm^2. In the latter case, *a*-GaAs was compared to *a*-Si and it was found that the two semiconductors behaved similarly. Both semiconductors had a Rayleigh frequency decrease because of ion implantation, although for GaAs the decrease was ∼43% while Si had 22%. This difference does not negate the parallels seen because amorphous regions are produced by heavy-ion bombardment for both these materials.

Due to the similarities of GaAs and silicon in coordination and bonding, this inspired the utilization of the work of Zhang et al.[19] as a guide to study the elastic properties of GaAs. The method will be employed to determine the elastic constants of amorphous GaAs because these properties have not yet been established with SBS.

An understanding of the structural changes associated with ion implantation is crucial. It aids with the identification of the nature of the disorder. This is possible with Raman spectroscopy as it is vital in the interpretation of the elastic properties of solids derived from surface Brillouin scattering. Raman spectroscopy describes the inelastic scattering of light through the emission and absorption of optical phonons. It is a fast and convenient analysis method used to determine the structural properties of both crystalline and non-crystalline materials[20,21].

Due to the zinc-blende structure of crystalline GaAs, the corresponding Raman spectrum of the sample comprises two modes which are distinguished features, longitudinal optical (LO) and transverse optical (TO). These modes are associated with the Brillouin zone centre, and they obey the following selection rules: solids of this nature with a [100] orientation have a dominant LO phonon

peak while the TO phonon peak is forbidden. When the same solid has a [110] orientation the TO phonon peak becomes dominant while the LO phonon peak is forbidden and lastly when the solid has a [111] orientation both LO and TO phonons are allowed[22].

c-GaAs have long-range order arising from their repetitive periodic atomic structure over its whole volume. This, therefore, allows for the conservation of phonon momentum, ($q = 0$ momentum selection rule) resulting in an LO phonon mode with frequency $\omega = 292$ cm^{-1} whereas for an amorphous layer the conservation of momentum is relaxed ($q \neq 0$). In this case, all phonons are optically allowed, and the resultant Raman spectrum consists only of a broad band at $\omega = 250$ cm^{-1}. When ion implantation induces a structural transition to the amorphous or disordered phase, there are often intermediate states that accompany the transition. These structural states can also be observed during the recrystallization process. They start as a redshift of the LO phonon peak. For example, GaAs implanted with nitrogen at doses $6{\times}10^{15}$ and $2.2{\times}10^{16}$ ions/cm^2 with energy 60 keV, the LO phonon peak decreases in intensity and broadens while the TO phonon peak increases in intensity while also broadening[23]. Zallen[24] and Mohanta et al.[25] reported similar transitions for GaAs after having used different ions for implantation. They reported that ion implantation is the ideal method of inducing these intermediate states because with a controlled dose it is possible to produce a system composed of both nanocrystals and amorphous composites. Additionally, as the dose of implantation increases, crystallite sizes decrease causing the changes that occur to the LO phonon mode[20,24,26–28].

1.2 Problem statement

Ion implantation can alter the structural, physical, and in turn elastic properties of semiconducting materials such as GaAs. A lot of research has been conducted on studying the structural and physical properties of ion implanted GaAs to determine the implantation condition that produces the most damage[29–31]. However, the elastic properties of amorphous GaAs have not been established. The surface Brillouin scattering technique together with the surface elastodynamics Green's function make the determination of the elastic constants feasible. This requires establishing the thickness and the density of the amorphous layer, as a function of ion dose and energy using SRIM and X-ray reflectivity.

1.3 Aims and objectives of this study

This project aims to use ion implantation of argon ($^{40}Ar^{+}$) and silicon ($^{30}Si^{+}$) ions to induce a near-surface amorphous layer embedded on a [100] GaAs substrate. The implantations will be done as a function of ion energy to obtain layers of varying thicknesses. The ion doses will also be varied to obtain different degrees of disorder. The objectives are thus to:

- Quantitatively analyse the structure of the disordered system using Raman spectroscopy
- Use complementary techniques such as X-ray diffraction (XRD), grazing incidence X-ray diffraction (GIXRD) and X-ray reflectivity (XRR) to analyse the physical properties of the implanted and un-implanted systems.
- To determine the elastic constants of the amorphous layer using the surface Brillouin scattering method to obtain experimental data and the surface elastodynamics Green's function to extract the elastic constants.

1.4 Outline of the dissertation

The current chapter outlines the introduction and literature of the study. It also includes the problem statement and aims and objectives of the project. The second chapter focuses on the theoretical details of the surface Brillouin scattering technique. The third chapter presents material modification by ion implantation and experimental details of SBS, and complementary analysis techniques used in this project with their experimental details. In this respect, Raman spectroscopy, X-ray diffraction and grazing incidence X-ray diffraction and X-ray reflectivity are described. The fourth chapter presents the experimental and simulated data. This chapter also includes the analysis and discussion of these results. The summary, conclusions and outlook for future work are gathered in chapter 5, and it is followed by the list of references used throughout the dissertation.

Chapter 2

Surface Brillouin scattering (SBS)

This chapter describes the essential elements of the surface Brillouin scattering method. It starts with a synopsis of the method and proceeds to describe the theory of elastic constants, depending on whether the material is anisotropic or isotropic. Subsequent to that, is the summary of the scattering mechanism followed by the surface elastodynamics Green's function and how it links to SBS.

2.1 Theory of surface Brillouin scattering

Surface Brillouin scattering is defined by its ability to non-destructively probe the dynamics of acoustic phonons propagating on the surface of thin films to determine their elastic properties. Surface waves can be described as modes with elastic energy propagating parallel to the plane of the surface with a displacement amplitude decaying at an exponential rate with the distance into the bulk of the solid. The theory of elasticity is used to explain the dispersion relations and the vibration amplitudes of these waves[32,33].

Lord Rayleigh studied surface and localised vibrations of multilayered mediums using the propagation of earthquakes. Since then, the theory of surface waves was mostly used in seismology. In the early 1920's Brillouin and Mandelshtam independently studied inelastic light scattering. They reported that the interaction of light with thermally excited acoustic waves led to a frequency shift relative to that of the incident beam by an amount equal to the frequency of the mode responsible for scattering. The development of lasers saw to the success of Brillouin scattering. This scattering phenomenon uses monochromatic light to study different modes propagating in a material. The use of visible light in Brillouin scattering translates to measured SAW in the frequency range of a few

to 30 GHz[12]. The technique is especially suited to measure the elastic constants of thin films with thicknesses comparable to the wavelength of the light used[32,33].

2.1.1 Elastic constants

Acoustic waves propagate through compressions and rarefaction in gas and in crystals, they move through atomic vibrations. These vibrations displace particles, and in turn, their internal restoring forces acting together with the inertia of the particles leads to oscillatory motions in the crystal. Deformation in materials is described as particles having been displaced relative to each other. Strain is a measure of deformation. For infinitesimal displacements, it may be expressed in terms of,

$$S_{ij} = \frac{1}{2}(\frac{\partial u_i}{\partial x_j} + \frac{\partial u_j}{\partial x_i})(i, j = x, y, z), \tag{2.1}$$

where S_{ij} is the Cauchy strain tensor, u_i is the displacement vector and x_i is the position vector. Hooke's law states that strain is linearly related to stress for elastic deformations. This relation can be described by,

$$T_{ij} = C_{ijkl}S_{kl}, \tag{2.2}$$

where $i, j, k, l = x, y, z$, T_{ij} denotes the stress component, S_{kl} is the strain component and C_{ijkl} is the elastic stiffness coefficients. The elastic constant is a measure of how resistant a material is to elastic deformation. The constant will be large for rigid material and small for ones that can be easily deformed. Similar to equation 2.2, strain adopts relation,

$$S_{ij} = S_{ijkl}T_{kl}, \tag{2.3}$$

where S_{ijkl} is the compliance constant that represents a measure of deformability of a material. This constant is small for rigid material.

There are $3^4 = 81$ elastic stiffness coefficients and due to symmetries of solids, the number of elastic constants reduces. For instance, if a solid has two symmetrically equivalent directions the stresses along these directions are considered to produce an identical strain. This proves that the stiffness, (alternatively compliance) coefficient will be identical along the same directions. This relation,

$$C_{ijkl} = C_{jikl} = C_{ijlk} = C_{ijkl}, \tag{2.4}$$

brings down the number of independent constants to 36. The Voigt notation[34] can contract these indices using their interchangeability. The contraction is done by replacing each i, j and k, l with α and β, respectively, such that $i, j, k, l = 1, 2, 3, ...$ and $\alpha, \beta = 1, 2, .., 6$ through,

$$11 \rightarrow 1, 22 \rightarrow 2, 33 \rightarrow 3, 23 \equiv 32 \rightarrow 4, 31 \equiv 13 \rightarrow, 12 \equiv 21 \rightarrow 6. \tag{2.5}$$

This simplification leads to elastic constants adopting notation, $C_{ijkl} \rightarrow C_{\alpha\beta}$. Additionally, $C_{\alpha\beta} = C_{\beta\alpha}$. This means the diagonal of the elastic constant matrix is symmetric, leading to 21 independent constants. A material's symmetry will further reduce the number of elastic constants, for example, a cubic crystal has three independent constants while a hexagonal one has 5 and an isotropic solid has 2[35–37].

Acoustic waves are considered elastic waves. As the atoms vibrate the bonds stretch and relax with the movement. Different propagation directions give different vibrations for anisotropic medium. An elastically anisotropic system is defined by its elastic properties dependence on orientation. Cubic systems are an example of anisotropic solids with C_{11}, C_{12} and C_{44} as the independent elastic constants. When there are no external forces acting on an ideally anisotropic material, the equation of motion (EOM) for an elastic solid takes the form,

$$\rho(\frac{\partial^2 u_i}{\partial t^2}) = C_{ijkl}\frac{\partial u_k^2}{\partial x_j \partial x_l}. \tag{2.6}$$

If we assume a plane wave solution of the form,

$$u_i = U_i exp[i(kr - wt)], \tag{2.7}$$

where U_i refers to the polarization vector of the wave, k is the wave vector. A set of homogeneous equations - also known as Christoffel's equations, are obtained,

$$(\Gamma_{ik} - \rho\omega^2\delta_{ik})U_i = 0, \tag{2.8}$$

where,

$$\Gamma_{ik} = k_j k_l C_{ijkl}, \tag{2.9}$$

is the Christoffel tensor[2,38,39].

The displacements U_i are usually coupled for an anisotropic material and to find solutions to equation 2.8, the following secular equation must be solved,

$$D(k,\omega) = |C_{ijkl}l_i l_j - \rho\nu^2\delta_{jk}|. \tag{2.10}$$

Equation 2.10 presents the dependence of ω on $k = |k|$, furthermore, it characterizes the dispersion relation of the solid. For non-trivial solutions, the determinant of the coefficients must vanish, leading to the secular equation,

$$|\Gamma_{ik} - \rho\nu^2\delta_{ik}| = 0, \tag{2.11}$$

that is the cubic equation $\xi = \rho\nu^2$:

$$\xi^3 - A\xi^2 + B\xi - C = 0, \tag{2.12}$$

with $A \equiv \sum \Gamma_{ii}, B \equiv \sum(\Gamma_{ii}\Gamma_{jj} - \Gamma_{ij}\Gamma_{ij})/2$ and $C \equiv det|\Gamma_{ij}|$. There are numerical procedures that can be used to find the three roots of ξ. The three solutions that arise from the above velocity equation are related to mutually orthogonal wave polarizations. The one with the largest phase velocity (ν) is the general quasi-longitudinal while the two are quasi-transverse. They are known as the fast-transverse (FT) and slow transverse (ST) modes[2].

Equations 2.8 and 2.11 can be simplified along the high symmetry directions. For instance, when the wave normal lies in a crystallographic plane, of the three modes one becomes pure transverse with a polarization direction along the normal of the plane while the other two are mixed modes with polarization directions in the plane. Likewise, when the waves are normal to the crystallographic plane, of the three modes one becomes pure longitudinal with polarization direction along the normal and the other two modes become pure transverse[2]. Table 2.1 has the solutions to Christoffel's equation that give the phase velocities for the various propagation directions and their corresponding polarization directions.

Table 2.1: The phase velocity equations for cubic symmetry materials[2]

Propagation direction, **n**	Polarization direction, **U**	Wave mode	Velocity equation, $\rho\nu^2 =$
[100]	[100]	L	C_{11}
[100]	[010], [001]	T(2)	C_{44}
[110]	[001]	T	C_{44}
[110]	$[1\bar{1}0]$	T	$1/2(C_{11} - C_{12})$
[110]	[110]	L	$1/2(C_{11} + C_{12} + 2C_{44})$
[111]	$[1\bar{1}0]$, $[11\bar{2}]$	T(2)	$1/3(C_{11} - C_{12} + C_{44})$
[111]	[111]	L	$1/3(C_{11} + 2C_{12} + 4C_{44})$
$[\cos\theta, \sin\theta, 0]$	[001]	T	C_{44}
$(\cos\theta, \sin\theta, 0)$	(001) plane	qL, qT	$1/2[B \pm \sqrt{B^2 - 4C^2}]$

where $B = C_{44} + C_{11}$ and
$C = (C_{11}\cos^2\theta + C_{44}\sin^2\theta)(C_{44}\cos^2\theta + C_{11}\sin^2\theta) - (C_{12} + C_{44}^2\cos^2\theta\sin^2\theta)$.

2.1.2 Elastic wave propagation in isotropic solids

A material is considered isotropic if its properties are independent of orientation, when it possesses the same properties in all directions. Amorphous materials such as glass and polycrystalline metals are examples of isotropic materials. Moreover, for isotropic material shear stress is always

complemented by shear strain and the same is true conversely. Additionally, any transformation occurring in the x_1, x_2, x_3 axes have no effect on the stiffness and compliance tensors, therefore $C_{11} = C_{22} = C_{33}$, $C_{44} = C_{55} = C_{66}$ and $C_{12} = C_{23} = C_{13}$. This condition gives rise to the isotropic relation $C_{11} = C_{12} + 2C_{44}$ (equivalently $S_{11} = S_{12} + 2S_{44}$)[2,38].

For this class of materials, there are only two independent elastic constants, C_{11} and C_{12} and they are represented by Lamé constants λ and μ,

$$\begin{aligned} C_{12} &= \lambda \\ C_{44} &= \mu \\ C_{11} &= \lambda + 2\mu, \end{aligned} \tag{2.13}$$

and

$$C_{ijkl} = \lambda(\delta_{ij}\delta_{kl}) + \mu(\delta_{ik}\delta_{jl} + \delta_{il}\delta_{jk}). \tag{2.14}$$

The wave equation (2.6) remains true for isotropic materials. Moreover, it can be assumed that the waves propagate along the x_1 axes. With equations 2.8 and 2.11, the uncoupled displacements have equations,

$$\begin{aligned} \omega^2 U_1 &= (\lambda + 2\mu)k^2 U_1 \\ \omega^2 U_2 &= \mu k^2 U_2 \\ \omega^2 U_3 &= \mu k^2 U_3. \end{aligned} \tag{2.15}$$

For the non-trivial solutions, one of the equations in 2.15 becomes non-zero while the other two take the value of zero. When U_1 is non-zero, with its polarization vector parallel to its wave vector, the mode is known as the longitudinal mode and it has a phase velocity,

$$\mu_L = \frac{\omega}{k} = \sqrt{\frac{\lambda + 2\mu}{\rho}} = \sqrt{\frac{C_{11}}{\rho}}. \tag{2.16}$$

The two other modes with their polarization vectors perpendicular to their wave vectors, are known as transverse modes and they have phase velocity,

$$\mu_T = \frac{\omega}{k} = \sqrt{\frac{\mu}{\rho}} = \sqrt{\frac{C_{44}}{\rho}}. \tag{2.17}$$

When thermodynamic constraints are applied, the longitudinal mode is always greater than the transverse, $(\mu_L > (2/\sqrt{3})\mu_T)$[2,39].

The determination of elastic constants of materials from thermally excited surface acoustic waves is an important application of SBS. Here transverse and longitudinal acoustic (TA and LA) surface modes are a result of bulk waves reflected at the surface of the material and this is exploited. The Rayleigh SAW, which is localized at the surface, similar to the LA and TA waves, is related to the

bulk elastic characteristics, but more intricately. Consequently, the Brillouin spectrum comprises peaks from bulk excitations with severe broadening represented by a Lamb shoulder and surface excitations contributing to the spectrum[40].

2.1.3 Scattering mechanism

Surface Brillouin scattering is one of the many methods used to study the elastic properties of opaque thin films such as GaAs. The propagation of phonons on the surface of an opaque sample causes a dynamic corrugation otherwise called ripples.

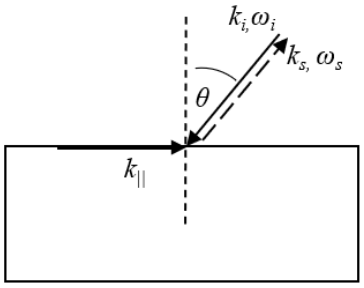


Figure 2.1: The wave vectors describing the interaction of the laser with a material.

When laser light with angular frequency ω_i and wave-vector component k_i is incident on the surface of a solid at angle θ to the normal, the beam will be reflected in a backscattering geometry for maximum momentum transfer, as seen in Figure 2.1. The wave vector of the surface waves is identical to that of the bulk waves parallel to the surface, suggesting that the bulk waves and the surface excitations caused by them are connected. The wave vector component of light perpendicular to the sample surface is not well defined due to the short penetration depth of light in opaque materials. Additionally, the beam will be inelastically scattered by the thermally excited surface corrugations with a wave vector parallel to the surface, $k_{||}$. There is a Doppler shift in the scattered beam giving it an angular frequency ω_s and wave-vector k_s and the change in frequency becomes $|\omega| = |\omega_s - \omega_i|$. As a result of $|k_s| \cong |k_i|$, energy and momentum conservation require,

$$k_{||} = 2k_i \sin\theta_i, \tag{2.18}$$

where θ_i is the incident angle. The velocity of the surface acoustic waves is thereby determined using the spectral frequency relation,

$$V = \frac{\omega}{k_{||}}. \tag{2.19}$$

The scattering cross-section for this mechanism is given by,

$$\frac{d^2\sigma}{d\Omega d\omega} = \frac{AT}{\omega} ImG_{33}(k_{||}, \omega), \tag{2.20}$$

for high temperatures, $T >> \hbar/k_B$, where $\hbar$ is Planck's constant, k_B is the Boltzmann constant, the factor A depends on the film, scattering geometry, frequency, and polarization of the incident light and $ImG_{33}(k_{||}, \omega)$ is the imaginary part of the surface Green's function[41,42].

2.1.4 Surface elastodynamics Green's function

The SBS measurements are usually taken as function of scattering angle, or azimuthal angle for c-GaAs, and amorphous layer thickness to derive phonon dispersion curves from the Brillouin spectra. Thereafter, the surface elastodynamics Green's function is applied to simulate the phonon dispersion curves to produce the elastic constants of the disordered layer. Green's function is also used to calculate the intensity of the surface Brillouin scattering spectra. Following closely the approach by Zhang et al.[19,39], consider a solid with the coordinate system adopted for the scattering as shown in Figure 2.2. The material will have thickness d corresponding to the opaque layer bonded to a substrate occupying the half-space $x_3 > 0$. The x_1, x_2 axes are parallel to the surface and x_1 is along the [100] direction, the x_3 is normal to the surface and in the [001] direction[19,39].

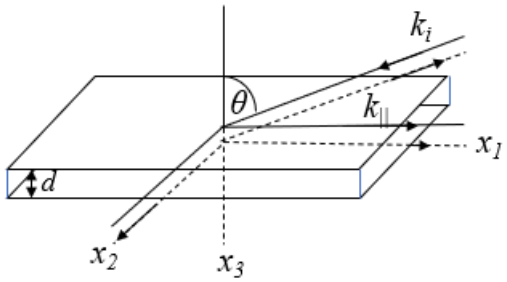


Figure 2.2: The scattering geometry of an SBS experiment.

Scattering is set to take place in the free surface (i.e., $-d < x_3 < 0$) given the opaque nature of the layer, if the film were transparent the scattering would be at the interface (i.e., at $x_3 = 0$). The cross-section for the scattered light is proportional to the power spectrum of thermal fluctuations in the normal displacement of the surface as given by,

$$I(\omega) = D\frac{T}{\omega} Im[G_{33}(k_{||}, x_3 = -d, \omega)], \tag{2.21}$$

where D is the factor determined by the density, permittivity of the solid and the incident light frequency and its polarization. G_{33} is the surface elastodynamics Green's function at (x_3, x_3). It is a

function of the surface wave-vector component parallel to the surface $k_{||}$, the near-surface thickness ($x_3 = -d$), and the angular frequency ω. Green's function is a superposition of six partial modes and takes the form,

$$G_{33}(k_{||}, x_3 = -d, \omega) = \sum_{n=1}^{6} \frac{i}{\omega} (B^{-1})_3^{(n)} (U)_3^{(n)} exp[-ik_3^{(n)} d], \tag{2.22}$$

for B the boundary condition matrix, $U_3^{(n)}$ the polarization vectors of the six waves[19].

The boundary conditions are the continuity of the stress component and the displacement field at the free surface ($x_3 = -d$). When Green's function is evaluated, the stress component becomes a function of the surface variables, the surface wave-vector, omega and $x_3 = -d$. Furthermore, the displacement field for the substrate and layer must satisfy the EOM as described by equation 2.6. The EOM also consists of six partial waves which are real and complex roots of equation 2.11, with its corresponding polarization vector found using equation 2.8. The waves correspond to different wave-vector components $k_3^{(n)}$ for $(n = 1, 2, .., 6)$ which are perpendicular to the surface. The layer uses all six equations, while the substrate has three outgoing and three incoming waves. It only uses the three outgoing for $k_3^{(n)}$ for $n = 7, 8, 9$ while the incoming waves are disregarded. The outgoing waves can be homogeneous, with $k_3^{(n)}$ real and having ray vector $v = \partial\omega/\partial k$ going into the substrate, or they can be evanescent waves with $Im(k_3^{(n)} > 0)$, and have their amplitudes fall into the interior. The boundary conditions imposed lead to nine equations that are used to determine the partial wave amplitudes. Equation 2.22 uses six of those nine in the layer[19].

The surface elastodynamics Green's function is implemented using a FORTRAN based computer program developed by Professor A.G. Every to calculate the SBS spectra. Figure 2.3 shows an example of the spectrum obtained where the Rayleigh SAW, and Lamb shoulder are the modes obtained for the c-GaAs simulation.

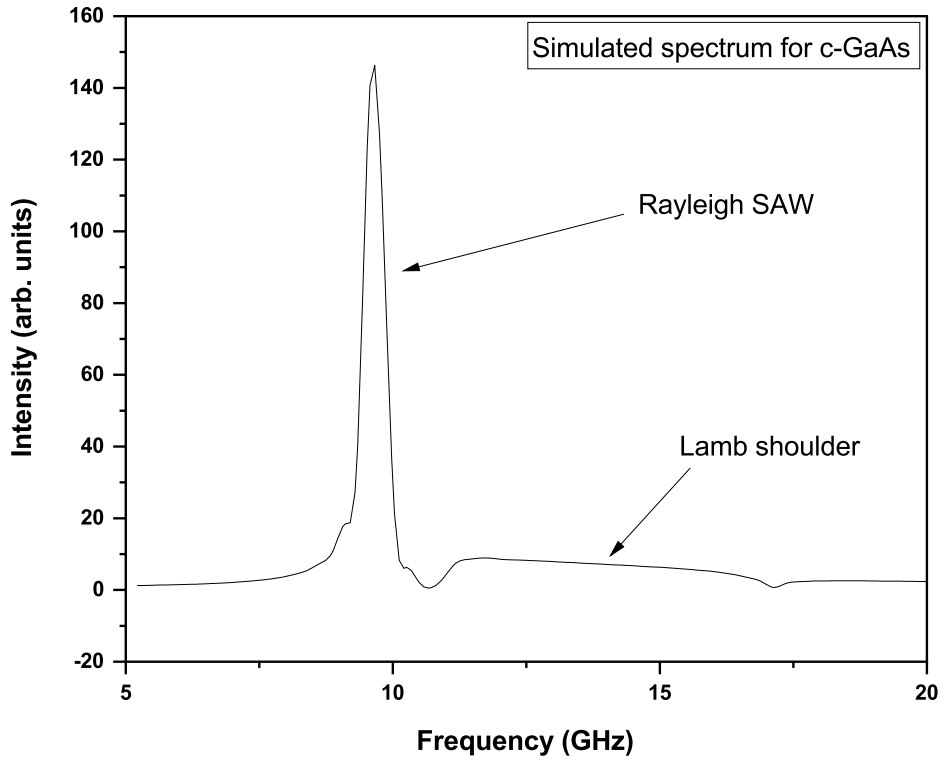


Figure 2.3: A simulation of the c-GaAs spectrum produced by the surface elastodynamics Green's function. This simulation was performed using literature values:[1] elastic constants $C_{11} = 120$, $C_{12} = 57.6$ and $C_{44} = 58$ GPa and density $\rho = 5.34$ g/cm^3 at incident angle of 71°

.

Similarly, the experimentally obtained SBS spectrum of c-GaAs is shown in Figure 2.4 where the sharp peak corresponds to the Rayleigh SAW mode in both the Stokes and anti-Stokes sides of the spectrum while the broad band is the Lamb shoulder.

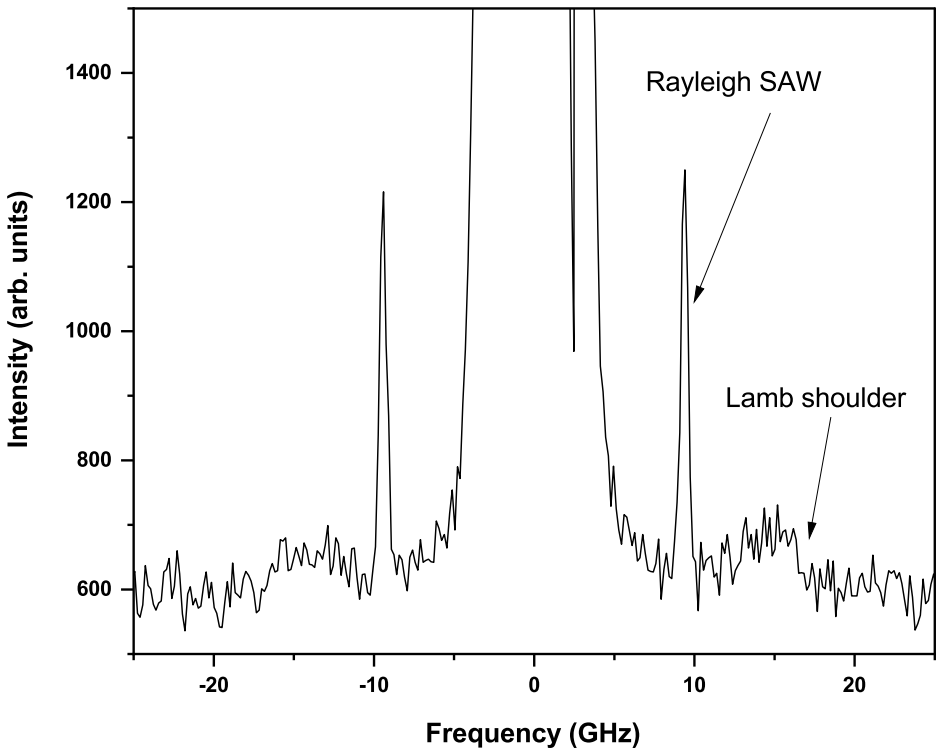


Figure 2.4: A typical measured SBS spectrum of c-GaAs showing the Stokes and anti-Stokes doublet. The peak at 0 GHz corresponds to elastic scattering obtained using the reference light source.

For a better representation of the peaks used for analysis (i.e., Rayleigh SAW and the Lamb shoulder) the peak that arises due to elastic scattering has been omitted. The features in the spectrum above were captured using an incident angle of $\theta = 68°$ and an azimuthal angle of $\varphi = 30°$. The specific experimental details employed during SBS measurements and complimentary techniques are discussed in Chapter 3 following the discussion on material modification by ion implantation.

Chapter 3

Material modification and experimental details

Material modification of GaAs wafers to realise amorphous layers of different thicknesses was undertaken using ion implantation. An introduction to ion implantation and parameters employed are presented in this chapter. Surface Brillouin Spectroscopy as the main technique together with supporting characterization methods are employed for determining the elastic constants, the density, thickness, and orientation of GaAs. The experimental details of SBS and complimentary techniques are discussed in this chapter. These additional characterization methods include Raman spectroscopy, X-ray diffraction (XRD), grazing incidence X-ray diffraction (GIXRD) and X-ray reflectivity (XRR). In addition, specific experimental details of each techniques and a short introduction of the working principle is given.

3.1 Ion implantation

Ion implantation is a technique used to modify a material's crystal structure by introducing dopants which in turn tune its electronic, magnetic, and optical properties. Ion implantation as a modification technique has proven itself as an integral part of materials processing, particularly in the semiconductor industry. Some of the advantages of this method include great accuracy in doping and control over the implantation depth. Moreover, it offers a wide range of dopant atoms that can be introduced, and solubility limits can be overcome. The dopants are in the form of charged particles that can be incorporated with tunable energies and doses for specific applications. The energy of the ions and the target material usually determine the penetration depth. The technique

has been employed in semiconductors to induce p-type and n-type doping which played a vital role in many technological applications. Furthermore, heavy, and energetic ions used in ion implantation induce lattice damage making it the ideal technique for studying amorphous materials[43–45].

3.1.1 Principles of ion implantation

During implantation, a beam of ions with high energy is focused on the surface of the target material leading to a series of collisions with the target lattice atoms. These ions, for example, Ar^+, lose energy to the target material by creating damage to the bulk of the host lattice. The energy lost is a result of electronic, nuclear (or elastic collisions) stopping and radiolysis (or photochemical processes). The former occurs when charge states change due to the deposited energy, however, this process does not include ionic displacement defects. Elastic or nuclear collisions are a result of momentum and energy transfer displacing atoms from their lattice positions. Radiolysis, occurs when a succession of reactions are set off by electronic excitation leading to the formation of atomic defects. The ion-solid interaction can lead to the ions probing the layers beneath the surface and producing a new 'arrangement' of atoms in the near- and sub-surface regions. Depending on the study undertaken or desired application, annealing using a furnace or laser is employed to restore the crystallinity of the lattice and to electrically activate the dopant ions[46,47].

In some cases, when ions with high energy are bombarded onto a crystalline target they can penetrate and tunnel through the open spaces between rows and planes of atoms. This occurs when they are incident in low index crystallographic directions. This phenomenon is called the channeling effect. The channeling effect is undesirable as it produces the least amount of implantation induced damage. In most ion implantation experiments, this is minimized by positioning the crystal off-axis with respect to the incident beam by a 7° tilt angle[48,49].

All the GaAs samples were implanted at iThemba labs Gauteng using the Varian 200-20A2F ion implanter. The ion sources are plasma generators that produce ion beams. The implanter at iThemba labs uses the Freeman Arc Discharge ion source since it can provide ion beams of almost any species (from solids to gases). The process of producing an ion beam has multiple steps namely, the gaseous (or solid) ion source chamber, vaporizer, gas feed system, extraction electrodes, cooling system, vacuum system, and power supply. Ion beams for implantation can be created using either a gaseous or solid source. By feeding gas into the ion source chamber, a beam is formed. A tungsten rod is heated to white-hot by a high filament current of 160 A in the ion source chamber to produce electrons via thermionic emission. These electrons collide with certain gas molecules, ionizing the gas and resulting in the formation of plasma. In the arc chamber, the ions created by a feed-through

are dissociated and ionized, then accelerated from the ion source to the analyzer magnet by a 23 keV extraction potential. The beam is focused with the help of a second 2 keV electrode. Since the ions at this stage are a mixture of isotopes and different fractions of molecules, the mass analyser exposes them to a magnetic field responsible for selecting the required ions utilizing mass analysis selection. Thereafter, they are directed to the accelerator tube that ensures the beams have the energy required for implantation. Here a radio frequency electric field is used to accelerate the ions to higher energy. These high and mono-energetic ions are then focused and scanned over the target material creating layers, in this case, of amorphous GaAs on a crystalline substrate. The implantation was performed at room temperature in a high vacuum (10^{-5}- 10^{-7} torr) environment to prevent contamination.

3.1.2 Ion implantation parameters and simulations

A wafer of single crystal [100] GaAs was used for implantation with singly charged argon ($^{40}Ar^{+}$) and silicon ($^{30}Si^{+}$) ions at different doses and energies. These wafers were acquired from Semiconductor wafer inc.[50]. They had a diameter of 50.8 mm and a thickness of 0.35 mm before slicing them into smaller pieces of about 6×5 mm^2 and implanting using the conditions listed in Table 3.1. The hypothesis is, while all the implantation parameters in Table 3.1 create a disordered layer on top of a crystal substrate, the damage induced by the controlled ion dose produces layers with different degrees of amorphousness. Additionally, the damage induced from the ion energy implantation influences the depth of the amorphous layer. As the ion energy increases the damaged layer increases. Lastly, because ion mass contributes to the amount of damage created during implantation, the use of lighter ions such as silicon and argon at doses in the range of the amorphous threshold was ideal to create an amorphous layer of GaAs. The stable $^{40}Ar^{+}$ isotope was used for ion bombardment as well as the $^{30}Si^{+}$, the latter was utilized to avoid nitrogen contamination.

Table 3.1: The ion implantation conditions used on (001) GaAs.

Ion dose (ions/cm^2)	Ion energy (keV)	Ions
1×10^{14}, 5×10^{14}, 1×10^{15}, 5×10^{15}, 1×10^{16}, 5×10^{16}	100	$^{40}Ar^{+}$, $^{30}Si^{+}$
1×10^{16}	30, 60, 90, 120, 150	$^{40}Ar^{+}$, $^{30}Si^{+}$

Stopping and Range of Ions in Matter (SRIM \TRIM)[51] simulations were performed to estimate the thickness of the disordered layer. The simulations were carried out using parameters matching those of ion implantation. Further, to acquire good statistics 10^6 ions were used in the simulations. Figure 3.1 shows the results obtained from these SRIM calculations. The values found were extracted using

the straight-line extrapolation of the deep-edge tail[19] and listed in Table 3.2.

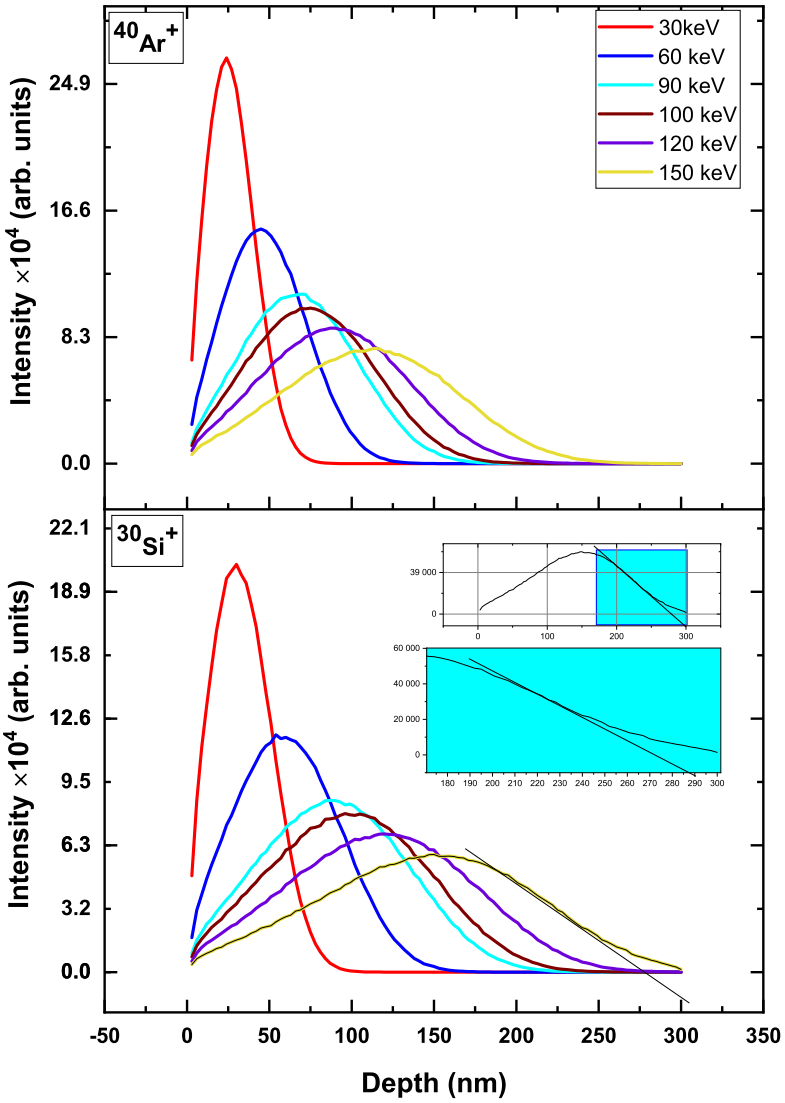


Figure 3.1: SRIM simulations of the depth profiles of GaAs implanted with $^{40}Ar^{+}$ and $^{30}Si^{+}$ with energies ranging from 30 - 150 keV.

Table 3.2: Tabulated SRIM thicknesses obtained from the two figures above.

Thicknesses (nm)		
Implantation energy (keV)	$^{40}Ar^{+}$	$^{30}Si^{+}$
30	60	75
60	120	137.5
90	150	190
100[a]	162.5	212.5
120	187.5	245
150	225	287.5

[a]The 100 keV implantation energy was used in conjunction with the varied ion doses as described in Table 3.1.

From Figure 3.1, the thin films created with constant energy (and varying doses) are projected to have the same thicknesses - 162.5 nm and 212.5 nm for argon and silicon ions respectively - while those implanted with different energies will not.

3.2 SBS experimental details

SBS is an optical technique that is used to study the elastic properties and acoustic excitations of thin films, multilayered and bulk materials. This is done by analysing the inelastic scattering of a monochromatic beam of laser light by acoustic phonons. The theoretical background of the technique is in chapter 2. This section contains the experimental details as carried out on the implanted and un-implanted thin films described in section 3.1.

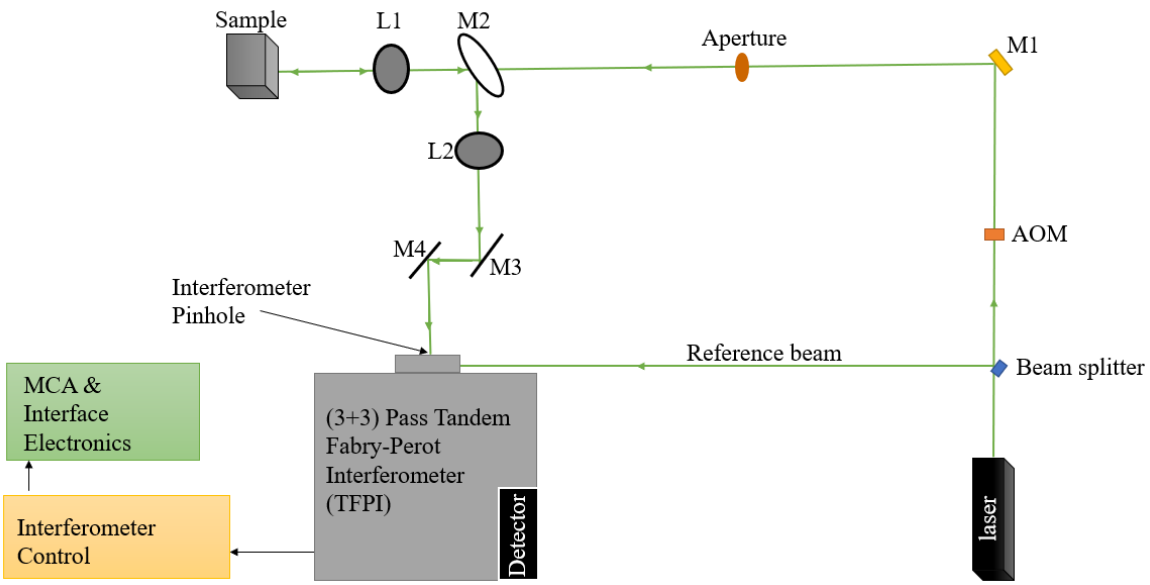


Figure 3.2: The external SBS experimental set-up showing the path travelled by the beam to the interferometer.

Figure 3.2 shows the schematic diagram of the SBS experimental set-up. The green lines depict the path traversed by the laser beam from the source to the interferometer, through the optical components and the reference beam. The basic requirements for any surface Brillouin scattering experimental set-up are therefore a monochromatic light source (i.e., laser), a high contrast Fabry-Perot interferometer, the optical components for the backscattering configuration, a sensitive detector, a multichannel analyser (MCA) and a computer for data capturing.

All the SBS experiments reported made use of the torus 532 Diode Pumped Solid-State (DPSS) laser at a wavelength of 532 nm which has a power output of up to 750 mW. The torus laser has a single longitudinal mode (SLM) and has electronic circuits designed to keep track of the longitudinal mode position to prevent mode hopping. The integral SLM operation is ascertained by the torus system acting as a travelling wave cavity. With the aid of the cavity's locking process and the power supply electronics, the SLM is actively confined to the peak of the gain profile. Another advantage of the travelling wave cavity is the low noise output of the laser.

In Figure 3.2, the laser light is split into two by a beamsplitter, and of the two, the reference beam goes directly into the interferometer. The other beam will be incident on the sample, it goes from the beamsplitter to the acousto-optic modulator (AOM). The AOM device is responsible for modulating the intensity of this beam. It will then pass through a mirror M1, an aperture, an elliptical mirror M2, a lens L1 and then it will reach the sample. The elliptical mirror has a 2 mm diameter aperture to allow the beam to pass through and a reflective side that redirects the beam

to the lens L2 in front of the walking mirrors (M3 and M4). The lens L1 has a focal point of 120 mm and it is responsible for focusing the beam onto the stage and collimating the light coming from the sample. These optical components are specifically placed for the backscattering geometry, as a result, the lens L1 receives the incident and backscattered light. The walking mirrors provide the advantage of degrees of freedom for the alignment process. These mirrors direct the beam to the interferometer.

The daily set-up consists of mounting the sample to the 3-axis translation stage with vertical rotations as seen in Figure 3.3. These vertical rotations ensure that variations in the incident angle are possible. For the crystalline samples, the incident angle was fixed at $\theta = 68°$ and the azimuthal angle ranged from $\varphi = 0 - 180°$. For the amorphous samples, the incident angle ranged from $\theta = 40 - 80°$ while the azimuthal angle was kept constant at $\varphi = 0°$. The samples are placed one at a time on the sample stage using double-sided tape.

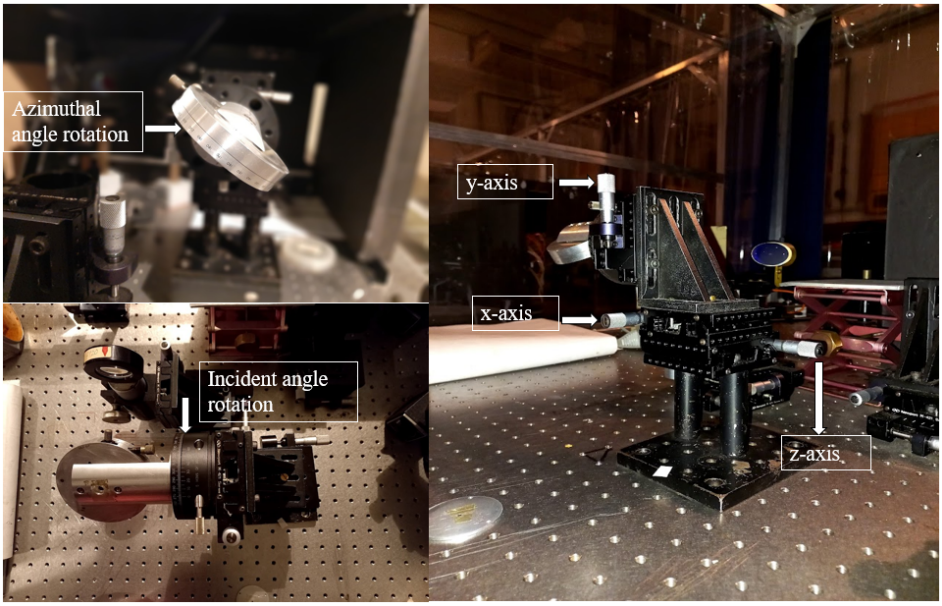


Figure 3.3: The 3-axis translation stage with azimuthal and scattering angle rotation.

When the beam reaches the pinhole, it will enter the Vernier-type tandem Fabry-Perot interferometers (TFPI) consisting of two interferometers in series such that their transmission functions overlap in a single spectral order. The Sandercock (3+3) pass TFPI (of JRS Scientific instruments) was used for all the Brillouin scattering measurements and the entire set-up is on a vibration isolated optical bench. The TFPI allows for measurements of low intensity inelastically scattered light which results in fractional frequency shifts compared to elastically scattered light. The inelastically scattered light frequency is measured in the GHz range.

The TFPI is made up of two sets of plane mirrors parallel with a distance that must always be

equally separated by an optical spacing of n_1. For this spacing, the interferometer will transmit a certain wavelength λ given by,

$$T = \frac{\tau_0}{1 + (\frac{4F^2}{\pi^2}) sin^2(\frac{2\pi n_1}{\lambda})}, \tag{3.1}$$

with τ_0 being the maximum possible transmission determined by the losses in the system ($\tau_0 < 1$), and F is the finesse, which is determined by the reflectivity and flatness of the mirror. Equation 3.1 demonstrates that only wavelengths satisfying,

$$n_1 = \frac{1}{2} p\lambda, \tag{3.2}$$

will be transmitted, where p = 0, 1, 2.. is the integer value.

For a given finesse F, the frequency intervals between successively transmitted wavelengths (i.e., the free spectral range (FSR) as given by $\Delta\lambda = c/(2n)$ and the width $\delta\lambda$ of a given transmission peak are related by,

$$F = \frac{\Delta\lambda}{\delta\lambda}. \tag{3.3}$$

This means the finesse is related to the FSR and the resolution. Further, it is limited due to the quality of the mirror substrates and coatings. The finesse will determine the maximum number of features that can be resolved in a specified FSR and the resolution.

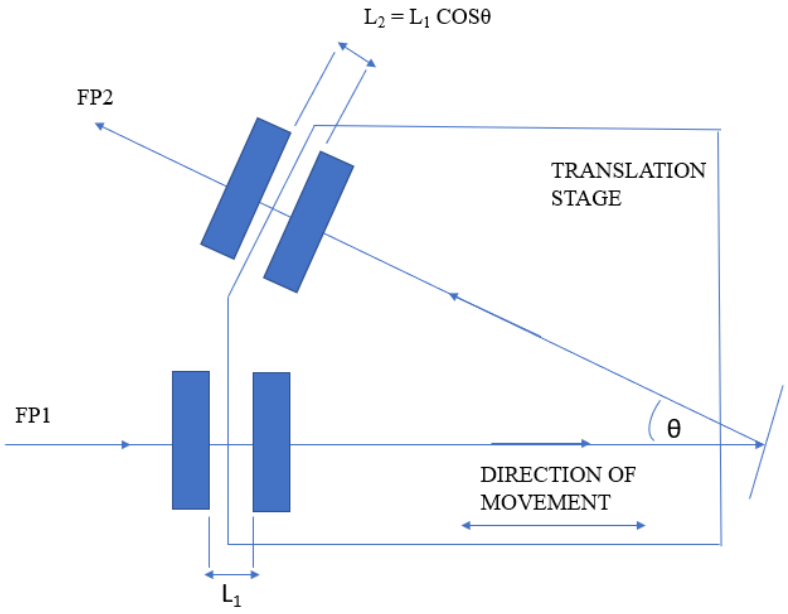


Figure 3.4: The geometry of the tandem interferometer.

Figure 3.4 illustrates the schematic of the two sets of parallel mirrors that make up the tandem interferometer. Both interferometers are mounted onto the scanning stage such that FP1 is along the translational stage movement while FP2 has an axis at an angle θ to the scan direction. The two

interferometers are arranged in this manner to achieve static and dynamic stable synchronization. When the interferometers move, the L_1 and $L_2 = L_1 \cos\theta$ spacing for the FP1 and FP2, respectively, is maintained to ensure a synchronous movement is achieved. This leads to a spacing of δL_1 and $\delta L_1 \cos\theta$, respectively, for a scan of the translational stage. An upper limit is imposed on the scan length by the displacement of the FP2 mirrors to ensure the mirrors always overlap. That is $D/\sin\theta$, where D is the diameter of the mirror, if the scan exceeds this limit the mirrors would no longer overlap.

The beam will be directed by a series of optical components in the interferometer such that it passes through each interferometer three times. The beam is then directed through a band pass filter and lens for final focusing. Thereafter, the beam will reach the single-photon detector.

The detector used was the EG & G optoelectronic Canada SPCM-200-PQ with a dark count of 1 per second. It is a high quantum efficiency silicon avalanche photomultiplier tube attached to the TFPI box. A cable feeds data to the computer-based multi-channel analyser (MCA) interfaced with the TFPI and detector. The MCA used a JRS Scientific instruments Ghost software that was responsible for calibration and spectra acquisition.

Due to the sensitivity of the detector, the TFPI box must be opened in a dark room to deprive it of any stray light. Usually, a few adjustments need to be made to the x, y, z knobs on the sample holder (in rare occasions the walking mirrors are adjusted too) for external alignment. The internal alignment can be done using the interferometer controls. Thereafter, a spectrum can be acquired. The run-time for each measurement was 18-24 hours.

3.3 Raman spectroscopy

Raman spectroscopy is used to investigate solids, liquids, solutions and even gases. This method is used to characterize the structure and composition of matter in detail using the inelastic scattering of light on a quantized molecular system governed by the Raman effect. C.V. Raman, an Indian physicist discovered the Raman effect in 1928. Raman spectroscopy is often referred to as vibrational spectroscopic technique due to the vibrational states of molecules being used as scattering systems. It serves as a complementary technique to IR absorption spectroscopy where the latter involves one photon absorption process while Raman includes two. In Raman spectroscopy, the emission and absorption of optical phonons constitute a Raman spectrum that comprises shifts in frequency both higher and lower than that of the incident beam. These shifts are called Raman bands and each of the bands is associated with the emission of phonons, in other words, Stokes scattering or

absorption of phonons, anti-Stokes scattering[21,52].

3.3.1 Principles of Raman spectroscopy

Raman spectroscopy is a fundamental vibrational spectroscopic technique used to obtain information on the structure and properties of materials. The Raman scattering process involves two photons, additionally, the change in polarizability of the material about its vibrational motion is the attribute in question. The polarizability interacts with the incoming radiation to form an induced dipole moment in the material, and the radiation emitted by this induced dipole moment contains the Raman scattering detected. Raman and Rayleigh scattering are both present in the light scattered by the induced dipole[53].

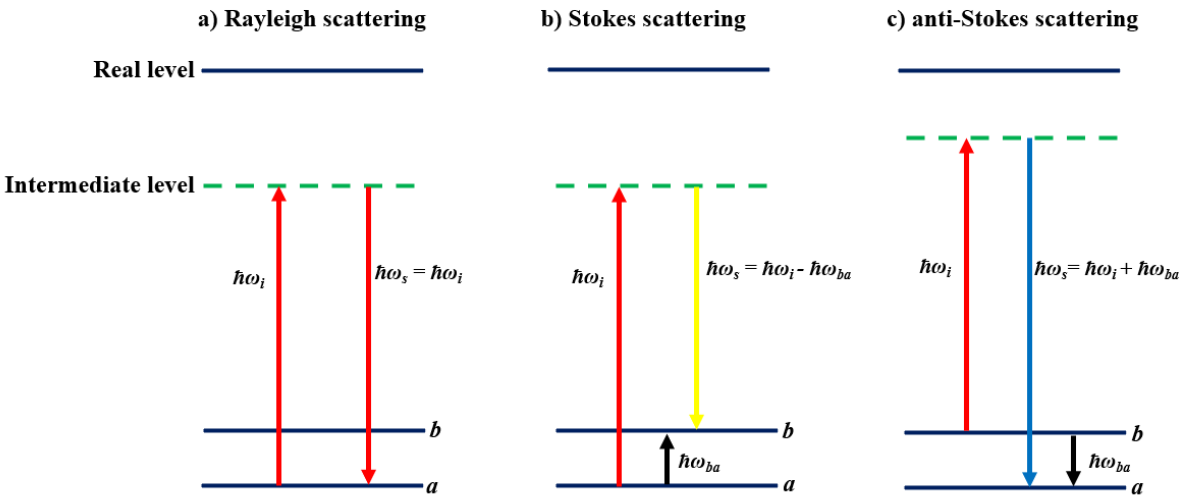


Figure 3.5: Energy diagram showing transitions for a) Rayleigh scattering, b) Stokes scattering and c) anti-Stokes scattering.

Rayleigh scattering is the elastic interaction of a photon with the medium where the frequency of the scattered light ω_s is equal to that of the incident ω_i, i.e., $\omega_i = \omega_s$. Raman scattering is inelastic, it results in a frequency shift, and hence energy, leading to either the absorption or emission of the incident photon. Figure 3.5 shows an energy diagram with the various events that lead to both Raman and Rayleigh scattering. The Raman method has Stokes and anti-Stokes scattering accounting for absorption and emission of some of the energy of the incident photon. Figure 3.6 has the Raman spectrum corresponding to these scattering events[53].

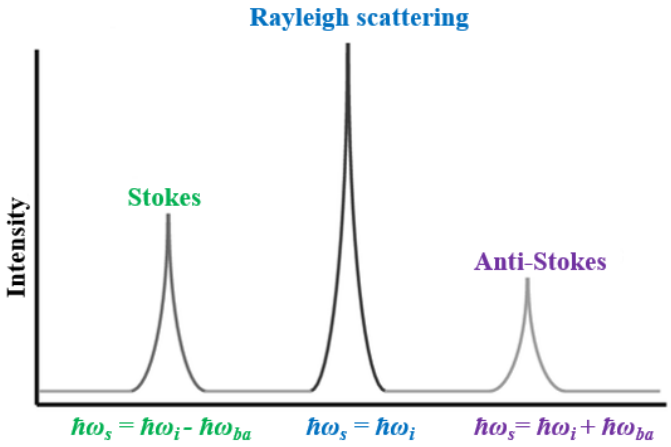


Figure 3.6: A Raman spectrum with Stokes, Rayleigh and anti-Stokes scattering lines.

The Raman spectra can be used to study the rotational level it is comprised of, thus leading to identifying the corresponding molecules making the sample. This makes it possible to use Raman spectroscopy for qualitative analysis. The intensity of the Raman line helps determine the concentration of a molecule in a particular sample, thus making quantitative analysis possible. Moreover, because the Raman intensity is a function of polarizability and symmetry it tests bonding covalence and structure directly, hence an investigation of the crystal to amorphous phase can be done[54].

Vibrational structure

Consider a crystal made up of unit cells where each cell had n number of atoms, this means it will have $3n$ vibrational branches. When the atoms in the unit cell move in similar directions as $q \to 0$, where q is the phonon momentum, they will have three acoustic modes, and when they move in opposite directions as $q \to 0$, they will have $3n$-3 optic modes. Symmetric crystals have three modes, one longitudinal and two transverse. The longitudinal mode has atomic vibrations along the phonon propagation direction while the transverse mode has vibrations that are normal to the direction of the phonon propagation. Polar semiconductors such as GaAs, have a triply degenerate structure at $q = 0$ that branches into doubly degenerate TO (transverse optic) phonon mode and a singly degenerate LO (longitudinal optic) phonon mode at higher energy[55].

Selection Rules

Raman spectroscopy measurements are mediated by selection rules which help identify modes while also limiting the experimental information. These rules are symmetry considerations that specify conditions for a phonon to be Raman active. For example, crystals with a centre of inversion can have Raman active phonons or infra-red active phonons depending on the symmetry of the crystal. This is due to crystals of this nature having an irreducible representation of phonons that can either be even or odd modes. Zinc-blende structures, such as GaAs, have an optic mode that is triply degenerate due to the deformation potential and electrostatic effects giving LO and TO modes that are Raman active. In the Raman experiment the LO mode scattering is observed from [100] and [111] oriented surfaces while TO mode scattering is observed from [110] and [111] oriented surfaces which produce first order peaks at 292 and 268 cm^{-1}, respectively. Diamond structures also follow the same selection rules as zinc-blende structured materials. On the other hand, metals usually have a single atom per primitive cell thus leading to them having no optic modes that can be Raman active[55,56].

3.3.2 Raman spectroscopy experimental details

The Raman spectra were recorded using a Jobin-Yvon spectrograph, an instrument that has many configurations making it possible for a range of samples to be analysed. Figure 3.7 shows the pathway of light for many configurations of the instrument.

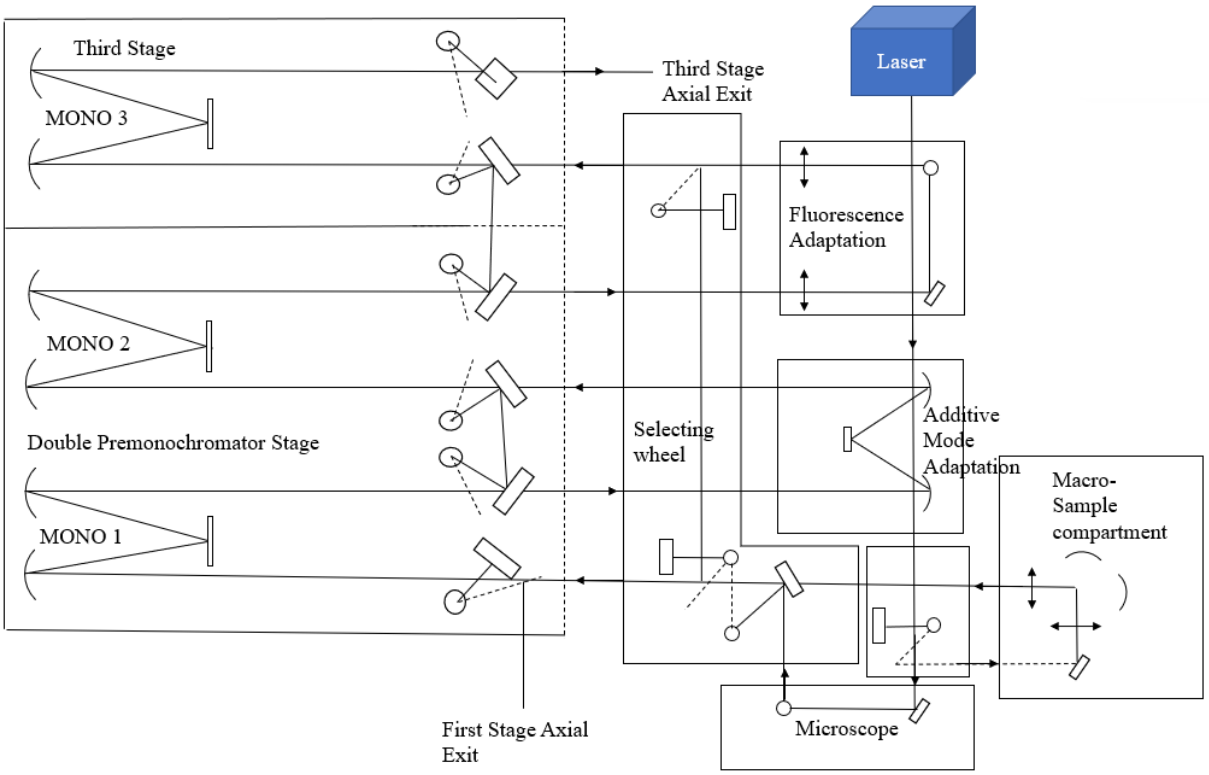


Figure 3.7: A schematic diagram of the Raman scattering experimental set-up.

The Coherent Innova argon ion laser was operated on a monochromatic wavelength $\lambda = 514.5$ nm leading to a penetration depth δ_p of,

$$\delta_p = \frac{1}{\alpha} = 1.107 \times 10^{-7} m = 110.7 nm, \tag{3.4}$$

where α is the absorption coefficient with magnitude 90.34×10^3 cm^{-1} for excitation energy of 2.41 eV on GaAs[57]. The laser beam is incident on the sample placed on a sample holder attached to the LabRam HR800-UV microscope connected to the spectrograph, therefore allowing for backscattering geometry of the incident light. The microscope has several objectives, the one used for these measurements was the $\times 100$ objective that has an N.A (numerical aperture) of 0.9 and a working distance of 0.21 mm. This objective gave the focused laser spot diameter of 0.7 μm on the surface of the sample. The sample stage is motorized and controlled by a computer thereby allowing the stage to move in the x and y directions. This feature together with the attached charge coupled detector (CCD) camera was beneficial especially for the $\times 100$ objective used because they were optical guides for placing the laser beam on the sample.

After the light is incident on the sample and backscattered it goes through an edge filter where inelastically scattered Raman light is selected by the selecting wheel (if the samples were bulky the light would be coming from the macro-chamber rather than the microscope). Following selection, the filtered light is dispersed using a single mode-spectrograph, the third stage spectrograph mono

3, with 1800 line/mm grating. The other options for dispersing light are the triple additive mode or triple subtractive mode. When light is dispersed with the triple mode, it must pass through the 'Additive Mode Adaptation'. The advantage of the single-mode spectrograph is it can produce data fast. A silicon-based CCD detector cooled in liquid nitrogen temperature, to ensure thermal noise is kept to a minimum, produces a photoelectron current that is proportional to the intensity of the radiation received by the detector. A computer is necessary to control the Raman spectrometer and spectra acquisition processes. It is also important for visualizing the produced spectra.

3.4 X-ray Diffraction (XRD) and grazing incidence X-ray diffraction (GIXRD)

X-ray based techniques have become the standard methods for studying the structure of the single crystal and polycrystalline materials. The techniques are based on the diffraction of X-rays by crystal planes in a particular manner allowing for a precise investigation of the structure of the crystal. The patterns are made up of contributions from micro-and macro-structural regions of a sample. Information on the lattice parameters, space group, chemical composition, macro-stresses and qualitative phase analysis can all be obtained using the peak position. Additionally, information on the crystal structure, texture and quantitative phase analysis can all be obtained from the intensity of a peak in an XRD pattern[58]. These techniques, namely, XRD and GIXRD are some of the X-ray based methods used in this project.

Diffraction occurs when waves pass through an aperture comparable to the wavelength such that interference patterns are observed. Diffraction of X-rays by crystals is related to phase relations of two or more waves such as phase differences caused by wave path length and a change in amplitude[59].

The main goal of X-ray diffraction by crystals is to determine the exact conditions in which X-rays scattered by atoms and those incident on a medium are completely in phase and reinforce each other resulting in a detectable diffraction beam. To illustrate, a common relationship between the X-rays incident and those scattered by the crystal are an integer multiple of the wavelength. Bragg's law, which includes the Bragg angle is the most essential and well-known approach for this purpose.

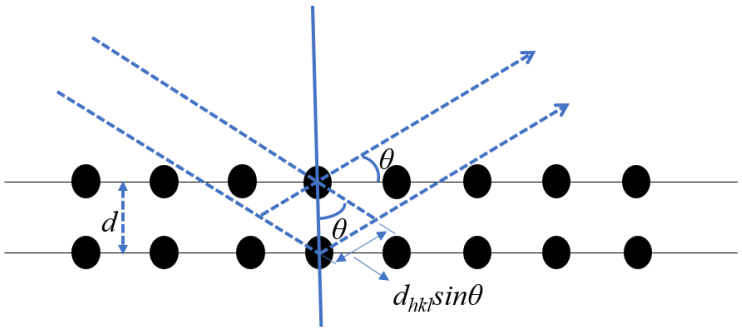


Figure 3.8: A schematic of X-rays incident on a crystal lattice where the black circles represent the atoms and the lines the imaginary planes.

Bragg's law is the mathematical representation of the X-ray diffraction event. As seen in Figure 3.8, if an X-ray beam with wavelength λ is incident on a crystal with its periodic arrangement and interplanar spacing d, a diffraction beam will be detected provided Bragg's law is satisfied,

$$n\lambda = 2d_{hkl}\sin\theta, \tag{3.5}$$

where n denotes the order of diffraction, λ refers to the wavelength of the incident photon and θ is the angle between the incident photon and the surface. When a material is polycrystalline, it has fine grains, this means diffraction will occur provided the lattice plane and direction satisfy Bragg's law[58,60].

Grazing incidence X-ray diffraction (GIXRD) is a surface sensitive technique as a consequence of its specialized scattering geometry. In a GIXRD experiment, the depth of penetration can be reduced leading to the maximization of diffraction signals from the surface, relative to the bulk. In this experiment, both the angle between the incident beam, the surface and the outgoing beam must be kept small while a diffraction pattern is being recorded. The acquisition process improves when the scattering angle increases when the X-ray tube and the detector are in proximity of the plane of the surface while scanning. As a result, the wave vectors of the incident and diffracted beams and the momentum transfer are restricted to the plane of the surface. The wave vector of the momentum transfer is the difference between the wave vector of the diffracted and that of the incidence, and it is almost perpendicular to the normal of the surface. Grazing incidence is different from a conventional XRD scan in that it investigates structure in the momentum transfer direction by exploring the interplanar spacing of perpendicularly inclined lattice planes[61,62].

The XRD and GIXRD measurements were conducted with the Bruker AXS D8 Discover X-ray diffractometer with a 2θ geometry. The X-ray diffractometer uses Cu-Kα X-ray source with wavelength $\lambda = 1.504$Å. Each sample is mounted individually onto the vertical stage where the suction

on the sample by the vacuum pump ensures it is fixed onto a motorized $x-y-z$ stage. The XRD measurements were recorded from 2θ = 20 - 80° in intervals of 0.008° while the GIXRD had an incident angle of $\omega_i = 1°$ for $2\theta = 3$ - 80° in steps of 0.06°. Prior to this scan, a series of optimization procedures are followed to ensure the measurements performed are reproducible.

3.5 X-ray reflectivity (XRR)

X-ray reflectivity uses grazing incidence X-ray beams to study the surface and interface roughness, density, and determine the thickness of a layered material. This X-ray technique is convenient in that it can be used to analyse materials that are either a single crystal, polycrystalline or amorphous[63,64].

The interaction of a beam of X-rays with matter is best represented by an index of refraction, which describes how the beam changes direction when travelling from air to a material. The refractive index, n, for X-ray radiation is written as follows,

$$n = 1 - \delta - i\beta, \tag{3.6}$$

where δ refers to the scattering and β to the absorption of the material. The refractive index of a material for X-rays is less than unity. When the X-rays are incident on a solid, they pass through air ($n = 1$) to the material ($n < 1$) causing total external reflection of the beam at small incident angles. The condition for the size of the incident angle is imposed by the critical angle, θ_c , defined by,

$$\cos\theta_c = n = 1 - \delta. \tag{3.7}$$

When the incident angle is less than the critical angle, total external reflection is observed. However, if it is equal or greater the X-ray will propagate on the surface or penetrate the material, respectively. Because n is slightly less than one, the Taylor series approximation makes the critical angle,

$$\theta_c = \sqrt{2\delta}. \tag{3.8}$$

As the angle of incidence increases above that of the critical angle, X-ray reflectivity decreases and so does the ratio of X-rays that are specularly reflected[63,64]. Figure 3.9 shows the geometry of an X-ray reflectivity measurement to attain in phase X-ray beam reflected from the surface of an over layer and the substrate.

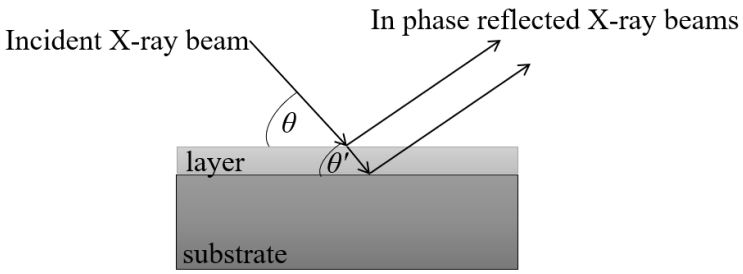


Figure 3.9: A schematic of the scattering that occurs in an XRR experiment.

As the beam of X-rays impinges on the surface of a flat material, a portion of their intensity is reflected while the other is refracted. The intensity of the reflected beam will propagate in the direction symmetric to the incident if the material is flat, i.e., specular reflection. On the contrary, if the surface of the material is rough the intensity of the reflected beam will propagate in many directions, i.e., diffuse scattering. The ratio of specular reflectivity is defined as,

$$R(\theta) = \frac{I(\theta)}{I_0}, \tag{3.9}$$

where $I(\theta)$ refers to the intensity of the reflected beam at angle θ, and I_0 to the incident beams intensity. For X-rays, the reflectivity is formulated as,[63,65]

$$R^{flat}(\theta) = |\frac{\theta - \sqrt{\theta^2 - \theta_c^2 - 2i\beta}}{\theta + \sqrt{\theta^2 - \theta_c^2 - 2i\beta}}|. \tag{3.10}$$

Figure 3.10 has an XRR spectrum of a multilayered material with oscillation referred to as Kiessig fringes where the red curve is simulated to match the experimental (black curve). The period of oscillations determines the thickness of the film, with the thicker film having a shorter period. LEPTOS software was used to perform this fit. With this spectrum, all the parameters (i.e., density, film thickness, roughness at the surface and interface) can be determined.

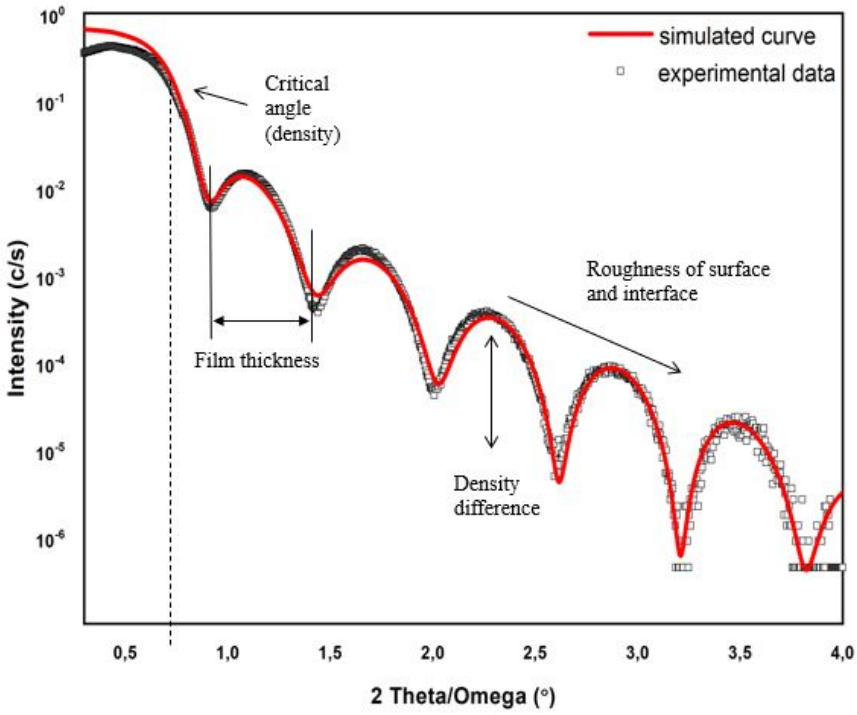


Figure 3.10: A typical XRR spectra with details on how the XRR parameters can be established.

On the other hand, Figure 3.11 shows the X-ray reflectivity curves of GaAs before, *c*-GaAs, and after implantation, *a*-GaAs, with Ar^+ at a dose of $1{\times}10^{16}$ ions/cm^2 with a constant energy of 100 keV. The shape seen in the figure is determined by the electron density ρ_e which can be converted to mass density ρ using,

$$\rho_e = \frac{Z\rho N_L}{M}, \tag{3.11}$$

where N_L is Loschmidt's number. Materials with high electron density usually have a high critical angle as a result of greater scattering intensity at higher angles. In the figure, the critical angle for *c*-GaAs was 0.58° while that of *a*-GaAs was 0.46°, this is a consequence of these samples possessing densities with magnitudes > 5 g/cm^3. In addition, the lack of Keissing oscillations could be attributed to destructive interference due to the surface corrugations of the amorphous layer on the crystalline substrate. The mass density was determined by a fitting with a simulation using LEPTOS software.

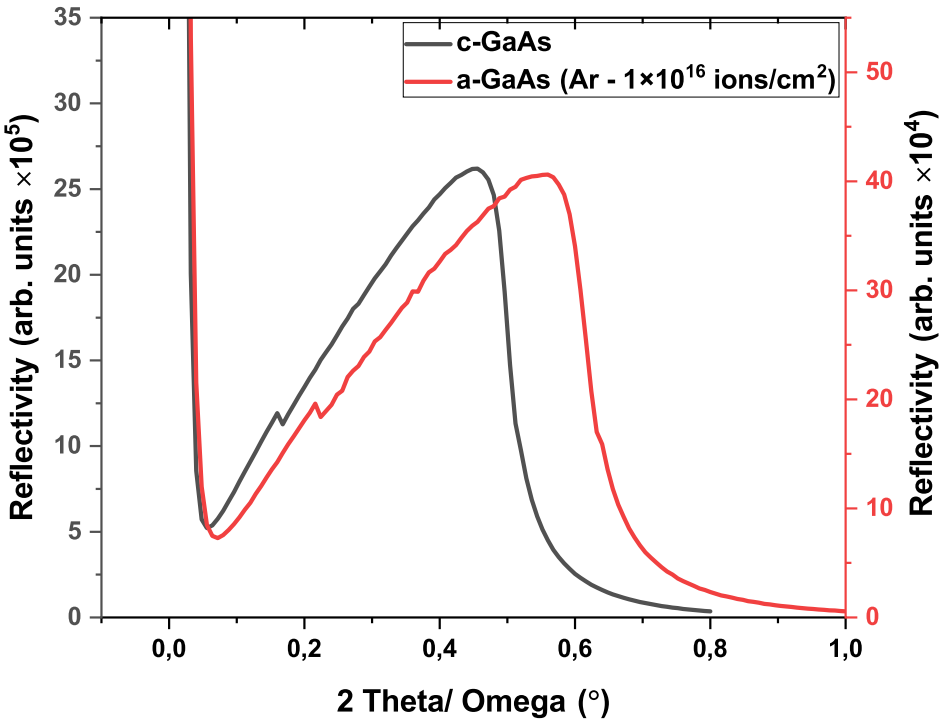


Figure 3.11: An XRR spectra of GaAs before, *c*-GaAs, and after ion implantation, *a*-GaAs: Ar^+ 1×10^{16} ions/cm^2.

The XRR measurements were also conducted with the Bruker AXS D8 Discover X-ray diffractometer that uses Cu-Kα X-ray source with wavelength $\lambda = 1.504$Å. For this measurement, optimization was carried out with the aid of sample height displacement adjustments and offsets in ω, and finally, a rocking curve at 2θ of 0.4° for specular reflection was done. Thereafter, the setting to a 2theta-omega scan was performed thus producing the required XRR spectra.

Chapter 4

Results and Discussion

The present chapter focuses on the results obtained prior and post ion implantation of (001) GaAs. The first section has the data obtained from the Raman spectroscopy characterization. The subsequent section presents the results obtained from the X-ray scattering measurements. These measurements were performed on crystalline and implanted GaAs samples to determine parameters such as density which is essential to SBS calculations undertaken to establish the elastic constants. Lastly, the results found from SBS measurements are presented together with the calculations for the elastic constants.

4.1 Raman spectroscopy

Raman spectroscopy is sensitive to the compositions, chemical environment, bonding and crystalline/amorphous structure of a material because it studies molecular and crystal lattice vibrations. First-order Raman scattering was used to distinguish between crystalline and amorphous GaAs due to the sensitivity of the Raman line to crystalline order.

The first-order Raman spectrum for single crystal (001) GaAs is identifiable by a single peak around $\omega = 290$ cm^{-1} [66]. This is due to the long-range order in c-GaAs allowing for the conservation of phonon momentum, i.e., the $q = 0$ momentum selection rule. The conservation of momentum is relaxed for amorphous gallium arsenide (i.e., $q \neq 0$). In this case, all phonons are optically allowed, and the resultant Raman spectrum consists only of a broad band at $\omega = 250$ cm^{-1} [20,66].

The Raman spectrum of (001) GaAs as seen in Figure 4.1 has two peaks, the dominant peak is associated with the LO phonons that arise due to scattering in a defect free crystalline sample. The

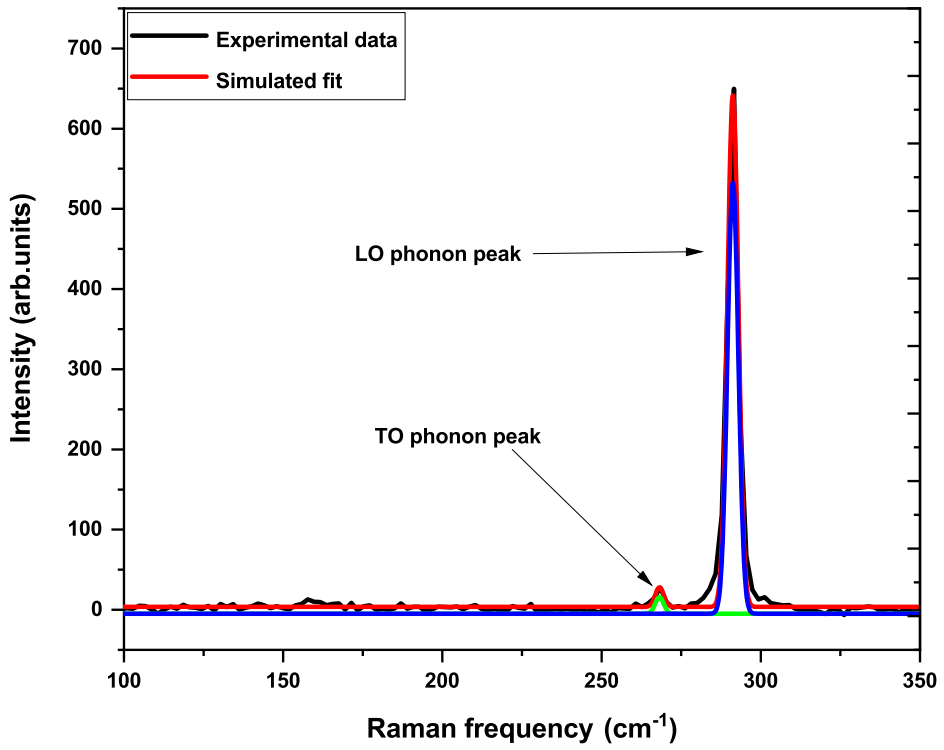


Figure 4.1: A Raman spectrum of c-GaAs with a simulated fit (red). The spectrum has an LO phonon peak (blue) at 291.24 cm^{-1} and a TO phonon peak (green) at 268.18 cm^{-1}.

lower intensity peak observed is attributed to TO phonons. As per the selection rules for the [100] orientation of a zinc-blende structure, this peak is forbidden. The presence of these phonons could be a result of the k-vector of the incident light not propagating along the [100] direction[22]. It could alternatively be due to impurities. Several other publications[22,43,67] have reported this feature for the un-implanted GaAs sample.

An argon ion laser with excitation energy of 2.41 eV (514.5 nm) was used to record these spectra, this laser has a penetration depth of 110.7 nm for GaAs. For the samples implanted with 30 keV energy for both ions, it would have been expected that the spectra would have contributions from the substrate given their SRIM amorphous layer thicknesses of 60 and 75 nm, for argon and silicon implants respectively. These spectra only showed records of the amorphous layer suggesting that the measurements were indeed taken at the surface of the sample.

4.1.1 Argon implanted GaAs

After ion implantation with $^{40}Ar^{+}$ ions using doses ranging from 1×10^{14} to 5×10^{16} ions/cm^2 at 100 keV the spectra in Figure 4.2a were obtained. Further, implantations with the same ions using energies 30 to 150 keV at a constant dose of 1×10^{16} ions/cm^2 were carried out and the spectra in

Figure 4.2b were obtained. The spectra in the figure were deconvoluted to find the peak features giving rise to the broad bands and symmetry peaks observed. There were bands with Raman frequencies below 200 cm^{-1}. These bands are attributed to II A phonons[26,67]. In Figure 4.2 the bands from these phonons were weak and broad.

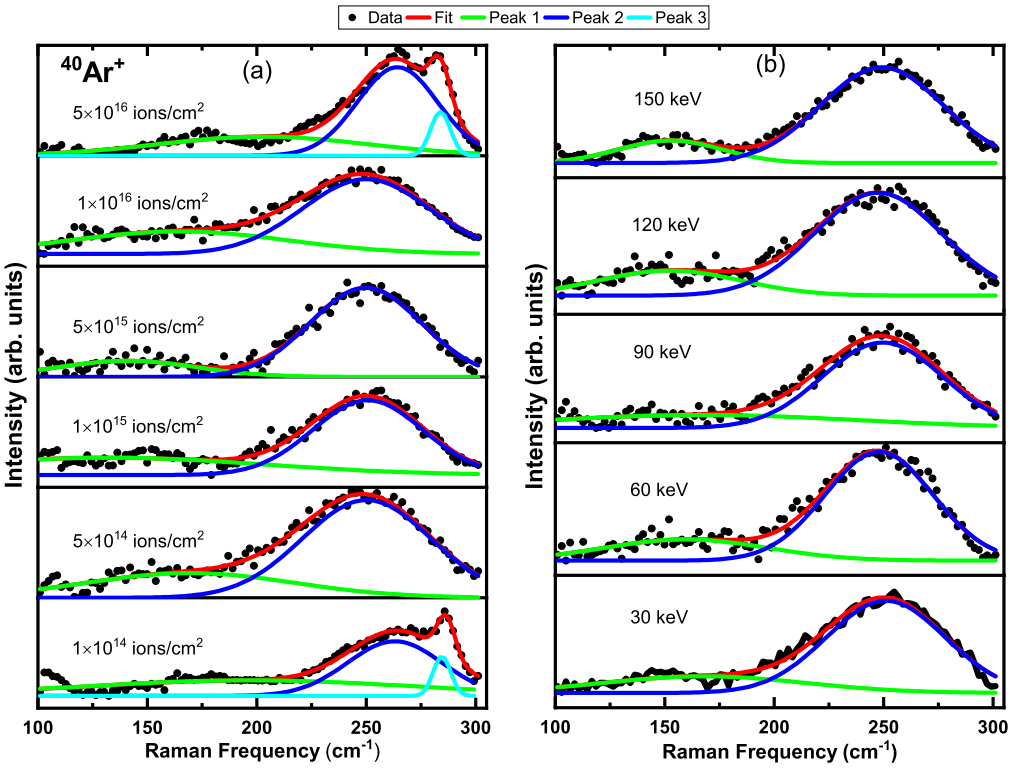


Figure 4.2: The Raman spectra of argon implanted GaAs where a) shows the spectra of the samples implanted with different ion doses while b) shows the spectra of the samples implanted with varying energies.

Comparing the spectrum of the sample implanted with 1×10^{14} ions/cm^2 to that of the (001) GaAs, the peaks are red shifted and broadened from 291.24 and 268.18 cm^{-1} to 285.42 and 263.79 cm^{-1}, for the LO and TO phonons, respectively. The full width at half maximum (FWHM) of the crystalline GaAs sample was 4.02 and 3.17 cm^{-1} and those of the 1×10^{14} ions/cm^2 implantation were 9.39 and 50.97 cm^{-1}, respectively. The redshift and broadening observed are attributed to partial amorphization due to implantation with a low dose[68]. An additional feature is seen in other implanted samples, it is a broad and asymmetric peak, located around 250.18 cm^{-1}, usually related to the damage regions of the sample. This observed band is associated with the continuous-random network (CRN) structure indicative of an amorphous solid. There are reports of this band being a superposition of two amorphous bands comprising of a LO phonon peak at 220 cm^{-1} and a TO phonon peak at 260 cm^{-1} [20].

Additional peaks were obtained in one of the spectra in Figure 4.2a. These peaks are characteristic of *c*-GaAs domains. The sample implanted with ions of dose 5×10^{16} ions/cm^2 had an LO phonon peak appearing at 283.96 cm^{-1} while the TO phonon peak was broad and located at 264.29 cm^{-1}. The appearance of these symmetry peaks could be a result of self-annealing[69,70]. When ion implantation for GaAs is carried out at room temperature, the concentration of induced damage decreases compared to when carried out at a lower temperature, this is assumed to be linked to self-annealing competing with the generation of lattice disorder[71]. Broad Raman spectra representing complete disorder were obtained in Figure 4.2b for the samples implanted with various energies in the 30 to 150 keV range at a constant dose of 1×10^{16} ions/cm^2.

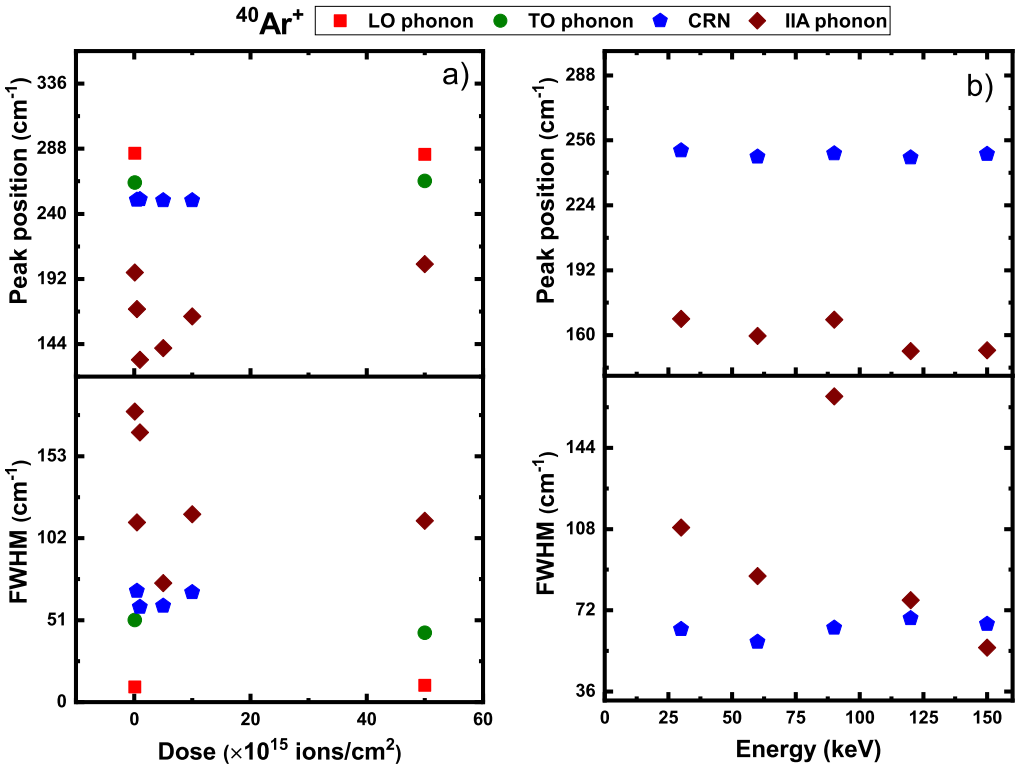


Figure 4.3: The FWHM and Raman position for argon implanted GaAs where a) shows the parameters as a function of dose and b) of energy.

Figure 4.3 shows all the trends for the samples implanted with varying doses (Figure 4.3a) and those bombarded with different energies (Figure 4.3b). The figure shows the LO phonon mode, appearing for the lowest and the highest dose (1×10^{14} and 5×10^{16} ions/cm^2, respectively) while not being observed for the other implantations. Argon is an inert ion, and when the implanted GaAs undergoes self-annealing it could result in the ions diffusing out of the layer leading to narrower peak shifts for the LO phonon mode, hence the smaller FWHM of 10.53 cm^{-1} observed for the highest dose. Further, a constant Raman frequency (peak position) is observed for samples with a CRN structure (5×10^{14} - 1×10^{16} ions/cm^2 samples) while the FWHM experiences a decrease from

the 5×10^{14} to 1×10^{15} and 5×10^{15} ion/cm^2 samples and an increase thereafter. Similarly, the II A phonons bands experience a steep decline in frequency for the first three doses and an increase afterwards for both the peak position and FWHM. The highest dose implantation which showed features of recrystallization is responsible for the peak position of the II A phonons of this sample being almost equal to that of the lowest dose. Likewise, the FWHM of the LO phonon modes are the lowest while those of II A phonons are the highest. For the samples implanted with varying energies, peak positions are not affected by ion energy. Additionally, the FWHM for II A phonons peaks decreases with increasing energy while those of the CRN are non-changing. All of these trends are a result of implantation induced damage as seen in Figure 4.2.

4.1.2 Silicon implanted GaAs

A different set of samples were implanted with $^{30}Si^{+}$ ions to form a disordered GaAs layer on top of a crystalline substrate. Figure 4.4a shows the Raman measurements collected from samples bombarded with different doses (1×10^{14} to 5×10^{16} ions/cm^2) while keeping the energy at 100 keV. In addition to this, Figure 4.4b shows the measurements for implantation at 1×10^{16} ions/cm^2 for the different energies (30 to 150 keV). The spectra in Figure 4.4 were also deconvoluted to find the peaks making up the experimentally obtained spectra.

Figure 4.4a shows the effect of varying the silicon dose on (001) GaAs. Using doses of 1×10^{14} to 1×10^{15} ions/cm^2 of Si^{+} created spectra showing the samples to be in the intermediate state. An intermediate state exists for implantation conditions that only create lattice disorder resulting in an atomic structure between the amorphous and crystalline form [24]. Again, the changes start with the LO phonon peak shifting to 285.41 cm^{-1} for the first three samples, coupled with a broad TO phonon peak at 262.67 cm^{-1}. These features represent contributions of the partial amorphous region induced by implantation. At doses around 5×10^{15} to 5×10^{16} ions/cm^2, only the CRN feature is observed, indicating amorphousness has been achieved. Several researchers [20,26,46,66] have studied the effects of silicon ions implanted on GaAs under similar conditions. Their results have shown the onset of amorphization at doses greater than 1×10^{15} ions/cm^2. In their reports, the implantation doses started at 8×10^{12} ions/cm^2 for a more comprehensive analysis of the LO phonon shift.

Figure 4.4b depicts a series of spectra showing the effect of changing the silicon ion implantation energy on GaAs. From this, only a broad peak located around 244.9 to 254.1 cm^{-1} indicating amorphization and loss of translational order was achieved. The sample implanted with silicon ions of energy 150 keV had an unforeseen result, similar to Figure 4.2a, symmetry peaks were recorded. The spectrum had a shifted LO phonon peak located at 283.2 cm^{-1} and a broad TO phonon peak

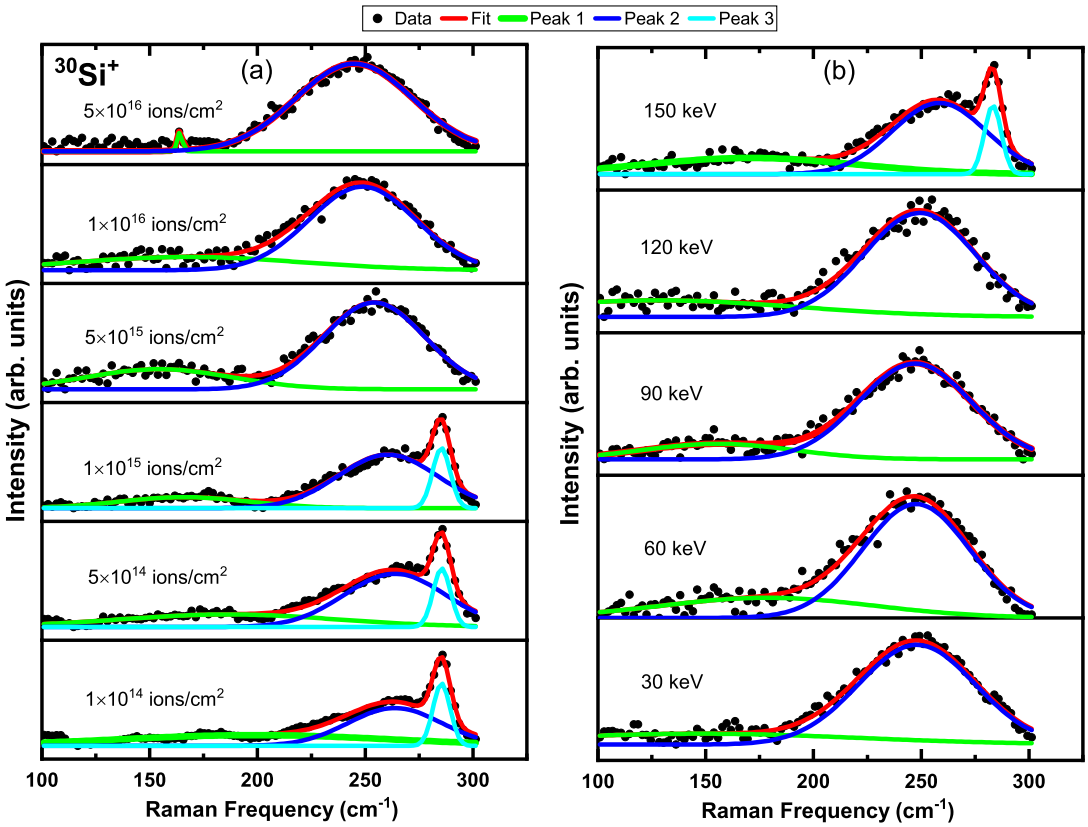


Figure 4.4: The Raman spectra of silicon implanted GaAs, where a) shows the spectra of the samples implanted with different ion doses and b) shows the spectra of the samples implanted with varying ion energies.

at 258.31 cm^{-1}. Usually, the process of self-annealing occurring during implantation is associated with high dose[69], in this case, it arose due to high energy bombardment. An imaging technique such as HRTEM could provide a more detailed description of the process occurring leading to the appearance of symmetry peaks.

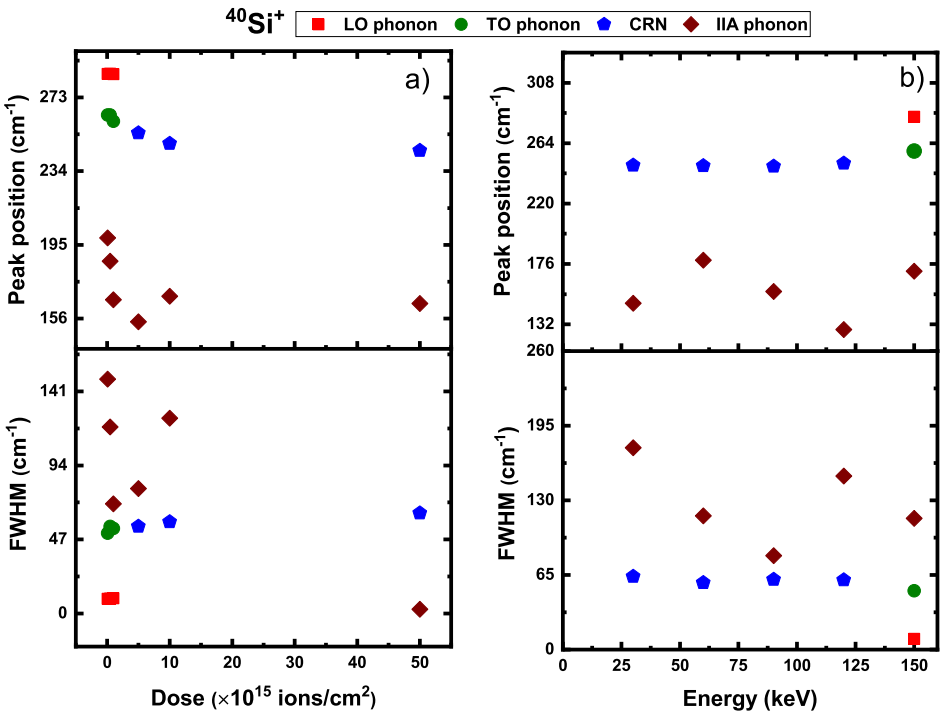


Figure 4.5: The FWHM and Raman position for silicon implanted GaAs where a) shows the parameters as a function of dose and b) of energy.

The changes in peak positions and FWHM for the silicon implanted (001) GaAs are presented in Figure 4.5. Here, it is observed that the FWHM for the samples implanted with varying doses increases with the peaks, where the LO phonon mode peaks had the lowest values and the II A phonons had the highest. In Figure 4.4a the three lowest dose implanted samples all had a shifted LO phonon peak, Figure 4.5a shows this as the clustered points (red squares for LO phonons) for both the peak position and FWHM. Further, in Figure 4.4a the same samples had broad TO phonon peaks, these correspond to the collection of three points (green circles) for both the FWHM and peak positions. The other data points are associated with the CRN band for the amorphous samples in Figure 4.4a. Similarly, the 150 keV implantation produced an outlier in the Figure 4.5b data. This is seen by the point with the lowest FWHM and the one with the highest peak position value. On the other hand, the CRN produced data points that were non-changing with increasing energy for both peak position and FWHM, except for the slight increase for the Si^{+} 150 keV sample. Lastly, the pattern obtained for II A phonon modes varied with the different energies. For energies 30 to 60 keV an increase for peak position and a decrease for FWHM are observed. Further, for FWHM the decrease stopped at 90 keV, thereafter increasing for 120 keV. The converse was observed for the peak position. It is clear that the implantation created clusters of disordered regions, whose sizes can be determined by grazing incidence to give a more comprehensive understanding of the FWHM changes observed especially for the II A phonon peaks.

4.2 X-ray diffraction (XRD) and grazing incidence X-ray diffraction (GIXRD)

Theoretically, the atoms in a single crystal are highly ordered forming a symmetric structure characterized by long range translational order. Therefore, a collimated beam of X-rays will be scattered by the electrons in the atoms to form a single diffraction peak that satisfies the Bragg condition. Figure 4.6 presents the XRD pattern of anisotropic GaAs in the Bragg-Brentano geometry using the Cu-Kα X-ray line. The diffraction pattern shows two prominent peaks at 31.64 and 66.05° constituting the multiplicity of the [100] planes. These peaks are assigned to the [200] and [400] planes corresponding to the zinc-blende structure of GaAs.

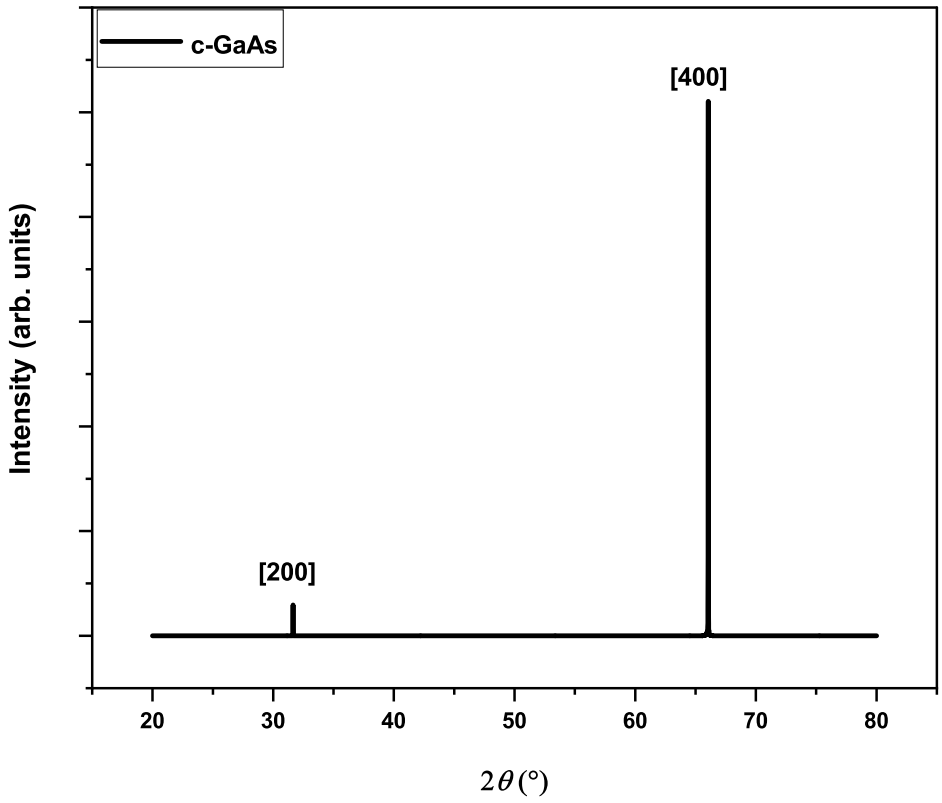


Figure 4.6: An XRD pattern of pristine GaAs.

Starting from the Bragg equation (3.5) the following relation,

$$\lambda = \frac{2a \sin\theta}{\sqrt{h^2 + k^2 + l^2}}, \tag{4.1}$$

was used to determine the lattice constant a of the crystalline GaAs and subsequently, its mass density, ρ_{GaAs}. λ is the wavelength of the X-ray Cu- Kα line, θ is the Bragg angle and hkl are Miller indices of the diffracting plane. The mass density has been determined to be $\rho = 5.319$ g/cm^3, this value is in good agreement to within 1% with literature which was $\rho = 5.317$ g/cm^3 [3].

After the confirmation of the orientation of the (001) GaAs substrate from the XRD measurement, implantations with argon and silicon ions to create an amorphous layered system on top of a crystalline were carried out. Due to the small thicknesses of the implanted layer, compared to the substrate, the conventional XRD beam could not be used to study these samples because of its large penetration depth and the randomized orientation of the grains/facets in the disordered layer. The penetration depth of X-rays for an incident angle greater than the critical angle is given by,

$$d = \frac{\sin\phi}{\mu}, \tag{4.2}$$

where ϕ is the incident angle and μ is the linear absorption coefficient [72]. GIXRD was thus employed as a surface sensitive X-ray technique to characterize the nature of disorder for the damaged layers of the various implantation conditions. For this technique, the standard Bragg-Brentano geometry is revised to give an 'asymmetric' diffraction result [73]. This means the angle of incidence is lowered therefore giving a smaller penetration depth thus making the technique surface sensitive.

GIXRD was performed on samples implanted with argon and silicon ions of doses 1×10^{14}, 1×10^{16} and 5×10^{16} ions/cm^2 at energy 100 keV (and 120 keV for silicon dose 1×10^{16} ions/cm^2). Figure 4.7 has the GIXRD patterns of the samples implanted with various argon and silicon doses. It is evident from the figure that the Bragg peaks appeared at angles 13.7, 16.5 and 53.5° corresponding to [111], [200] and [622] or [533], respectively. A closer look at this pattern revealed that even though the [111] and [200] peaks increase in intensity with increasing doses, their width does not exceed 1.3°. Further, other low intensity bands form for high doses of argon ion implantation. Similar bands were also observed for low dose and 1×10^{16} ions/cm^2 silicon. In Figure 4.7b for the implantation with dose 5×10^{16} ions/cm^2 a unique result is seen. The pattern revealed a dominant peak at $2\theta = 53.34°$. The other samples had peaks with weak intensities in the $2\theta = 53°$ region. In addition, this sample had a peak with weak intensity in the region of $2\theta = 16°$, whereas the other two samples had intense signals from this region.

The peaks in Figure 4.7 are an indication that even after implantation crystallites with the cubic structure of GaAs are still present in the samples and their low intensities can be attributed to a randomly distributed amorphous structure with crystallites. This result is corroborated by the Raman results found in section 4.1, where it was shown that damaged layers were created by ion implantation. Materials similar to GaAs with amorphous counterparts have been studied with GIXRD before, GaSb [74] and Ge [75] are some of these materials. The GIXRD patterns in these reports showed the material had reflections that satisfied the fcc structure of the crystalline material. For amorphous GaSb, the GIXRD peaks were very broad compared to Figures 4.6 and 4.7 and after annealing for the crystallization process, sharp signals were obtained. Additionally, for amorphous Ge, the patterns were of one sample with measurements taken at different angles.

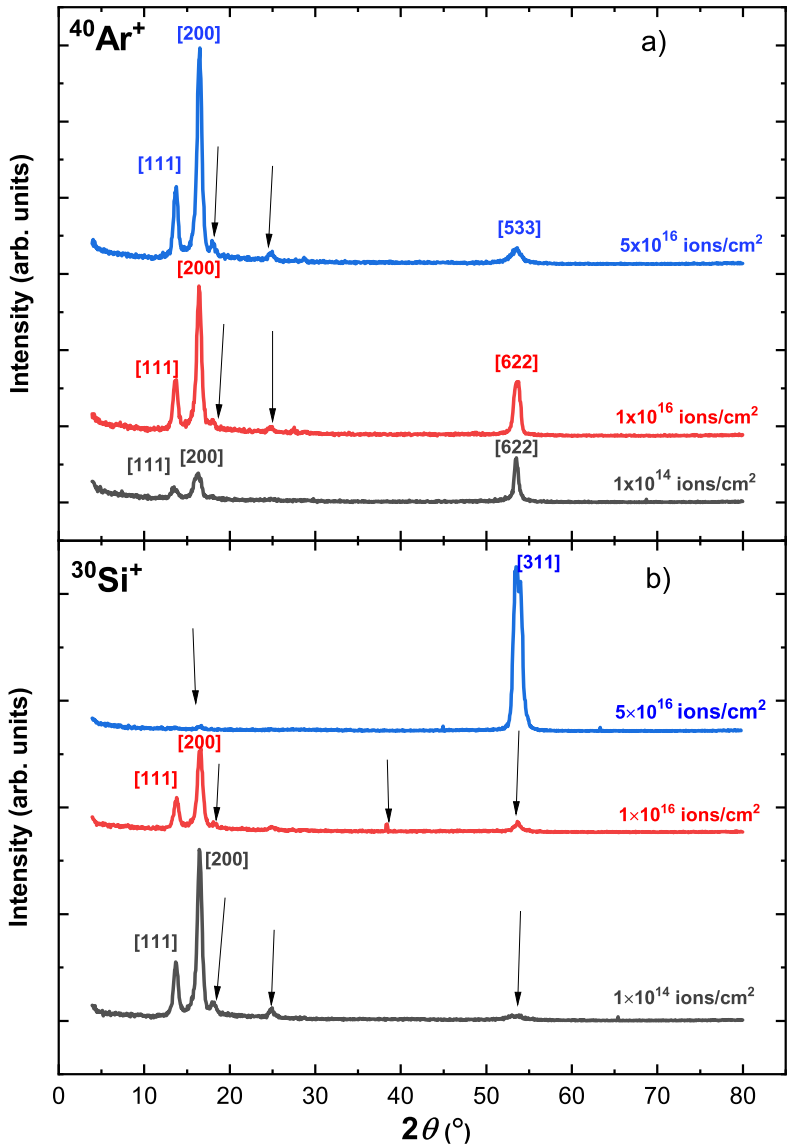


Figure 4.7: A GIXRD pattern of GaAs following implantation with a) argon and b) silicon ions of the lowest, second highest and highest dose taken at grazing incidence of $\omega_i = 1°$.

Using the Scherrer formula,[74]

$$D = \frac{0.9\lambda}{\beta \cos\theta}, \tag{4.3}$$

where $\lambda = 1.504$ Å is the wavelength of the X-ray beam, β is the FWHM of the Bragg peak and θ is the Bragg angle, the sizes of the crystallites can be determined. Table 4.1 has the calculated values, and it shows the crystallite sizes range from 1.04 to 7.92 Å.

Table 4.1: The crystallite sizes as determined by the Scherrer equation.

Sample	Peak	$\theta(^\circ)$	FWHM (°)	D (Å)
[a]*c*-GaAs	[200]	15.82	0.41269	3.40904
	[400]	33.024	0.20377	7.92292
a-GaAs - Ar 1×10^{14}	[111]	6.75	1.30275	1.04629
	[200]	8.16	0.85526	1.59887
	[622]	26.7	0.554456	2.78289
a-GaAs - Ar 1×10^{16}	[111]	6.78	0.87713	1.55408
	[200]	8.19	0.67994	2.01129
	[622]	26.88	0.95447	1.58996
a-GaAs - Ar 5×10^{16}	[111]	6.87	0.75489	1.80607
	[200]	8.25	0.77291	1.76961
	[533]	26.76	1.40415	1.07963
a-GaAs - Si 1×10^{14}	[111]	6.84	0.72830	1.87190
	[200]	8.22	0.68346	2.00107
[b]*a*-GaAs - Si 1×10^{16}	[111]	6.9	0.93335	1.46083
	[200]	8.31	0.68346	1.53009
a-GaAs - Si 5×10^{16}	[311]	26.82	1.1088	1.36793

[a]these peaks are from the XRD pattern

[b]energy 120 keV was used for this sample

The average size of the crystallites from implantations with argon ions are 1.81, 1.72 and 1.55Å for the 1×10^{14}, 1×10^{16} and 5×10^{16} ions/cm^2, respectively. Lastly, the samples implanted with silicon ions of doses 1×10^{14} and 1×10^{16} ions/cm^2 had an average size of 1.94 and 1.50Å, in that order.

4.3 X-ray reflectivity (XRR)

XRR was performed on both *a*-GaAs and *c*-GaAs using the D8 Discover Bruker AXS high resolution X-ray diffractometer. This was done to determine the density of the different *a*-GaAs samples. The samples chosen for this analysis technique were those implanted with argon ions of doses 1×10^{14}, 1×10^{16} and 5×10^{16} ions/cm^2. These samples were selected to corroborate their respective Raman spectra because they revealed partial amorphization for the lowest and highest implants and complete amorphization for 1×10^{16} ions/cm^2. Additionally, GaAs samples implanted with 30 and 150 keV argon ions were investigated. Samples implanted with silicon ions under similar conditions

were investigated for density estimation at the critical angle for total external reflection.

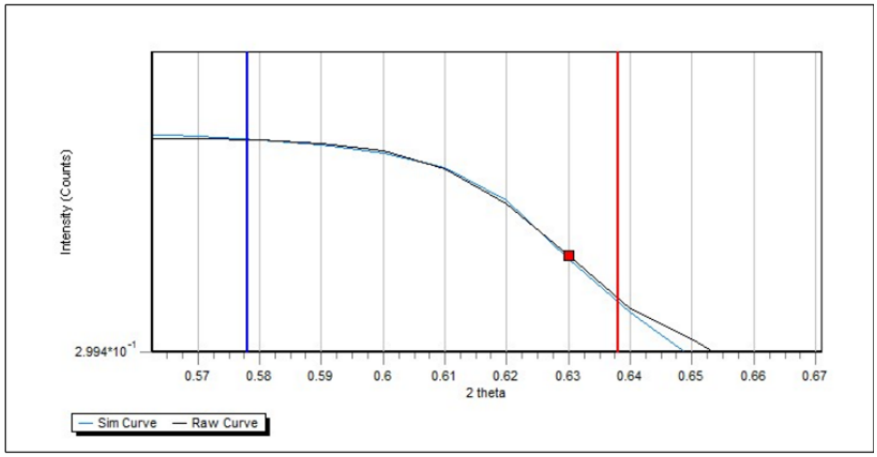


Figure 4.8: An example of the fit performed to establish the density of the un-implanted GaAs sample using LEPTOS.

A typical XRR spectrum provides the electron density, thickness, and roughness of the sample. These parameters are all obtained from the fringes in the spectra as discussed in section 3.5. The XRR spectrum for *c*-GaAs had no fringes owing to the bulk nature of the sample with similar electron density not providing an interface within the material to allow for constructive and destructive interferences of the X-ray beam leading to the formation of Kiessig oscillations. Similarly, the spectrum of *a*-GaAs did not show any fringes, however, density changes were obtained. These changes in density suggest the physical properties of the samples after implantation had indeed been altered. The spectra obtained were all fitted using LEPTOS at the critical point for total external reflection. Figure 4.8 depicts the experimental data (black) and the simulation (blue) assuming the layer stack *a*-GaAs/*c*-GaAs and the corresponding values of the density for the surface layer are listed in Table 4.2.

Table 4.2: The densities of a-GaAs as determined by XRR.

Sample	Density (g/cm^3)
c-GaAs	5.37137
Implantation with Ar^+ at varied dose (ions/cm^2) and energy (keV)	
a-GaAs - Ar 1×10^{14}	5.33837
a-GaAs - Ar 1×10^{16}	5.20245
a-GaAs - Ar 5×10^{16}	4.69019
a-GaAs - Ar 30	4.78700
a-GaAs - Ar 150	5.31877
Implantation with Si^+ at varied dose (ions/cm^2) and energy (keV)	
a-GaAs - Si 1×10^{14}	5.3232
a-GaAs - Si 5×10^{16}	5.26143
a-GaAs - Si 30	5.26976
a-GaAs - Si 120	5.27184
a-GaAs - Si 150	5.31410

The densities in the table above were averaged to obtain a density for the surface Brillouin scattering dispersion curve simulations performed to determine the elastic constants of amorphous GaAs. The average for the various doses of Ar^+ implantation was 5.08 g/cm^3. Additionally, for the same ion, the energy implantations produced a density of 5.05 g/cm^3. The silicon implanted samples densities were also calculated and it was found for those with varying doses and energies the value of 5.29 g/cm^3.

The densities of a-GaAs often vary with the modification technique used as well as the experimental conditions for the method. Reports using the evaporation as well as ion implantation techniques to create amorphous GaAs had density of a-GaAs as $\rho = 5.0 - 5.08$ g/cm^3 [76–78]. In these reports, the implantations are beyond those required for amorphization, compared to here where the conditions used were purely to create an a-GaAs system whilst also preserving the stoichiometry.

4.4 Surface Brillouin scattering (SBS)

A series of implanted GaAs samples and one un-implanted were investigated using SBS. The implanted samples were bombarded with $^{40}Ar^+$ and $^{30}Si^+$ using different doses and energies to create disordered samples as described in section 3.1. As per chapter 2, when the scattered laser light

interacts with the solid, frequency shifts equal to those of phonons created or annihilated are observed. The momentum and energy conservation determine the phonon wave vector, hence making the phase velocity of surface acoustic waves, $V = \frac{\omega}{k_{||}}$ where $k_{||} = 2k_i \sin\theta$. The samples implanted with varying energies had different thicknesses ranging from 60 to 225 nm and from 75 to 287.5 nm for Ar^+ and Si^+ respectively, thus giving different $k_{||}d$ values, where d is the thickness as determined by SRIM. This dimensionless quantity was plotted against the calculated velocities resulting in phonon dispersion curves. The phase velocities of the acoustic phonons in the curve are used to determine the elastic constants through the inverse problem method. The SBS method was used in conjunction with the surface elastodynamics Green's function to determine the elastic constants of c-GaAs and a-GaAs. The least-square fitting method was used to establish the errors in the results found.

4.4.1 Determining the elastic constants of single crystal GaAs

The Rayleigh SAW frequency varies with propagation direction in crystalline samples such as GaAs due to their anisotropic structure. For the single crystal (001) GaAs sample, measurements were carried out at different azimuthal angles, $\varphi = 0$ - 180° and an incident angle of $\theta = 68°$ to prove the existence of this surface anisotropy. Following closely the method outlined by Kotane[79] the data points in Figure 4.9 were obtained and fitted with a sinusoidal function to extract the [100] and [110] propagation directions. Figure 4.9 gives this dispersion curve, where only the two aforementioned propagation directions are seen. The [100] direction was taken as the reference and the [110] was found 45° from that position. The 3 elastic constants of single crystal (001) GaAs (i.e., C_{11}, C_{12} and C_{44}) can be recovered from SBS measurements obtained from the [100] and [110] directions. In addition to the Rayleigh SAW frequencies, the longitudinal and transverse acoustic modes are also needed. These are Lamb shoulder spectral features as seen in Figure 4.10. This measurement also shows that the from the results obtained, the uncertainty in the determination of the longitudinal and transverse acoustic modes is relatively high. The Rayleigh SAW, transverse and longitudinal acoustic frequencies were extracted for the two propagation directions and they are listed in Table 4.3. Figure 4.10 only shows the anti-Stokes side of the SBS spectrum, however, the quantities in the table below are averages of the Stokes and anti-Stokes frequencies. These values together with the density from the XRR measurement were used to determine the elastic constants for c-GaAs. The merit function previously described in Sumanya's Thesis[80] has been used to estimate the elastic constants from 3 values of the wave velocities measured for c-GaAs in the [100] for the h_1 and h_3 and [110] for the h_2 functions, respectively.

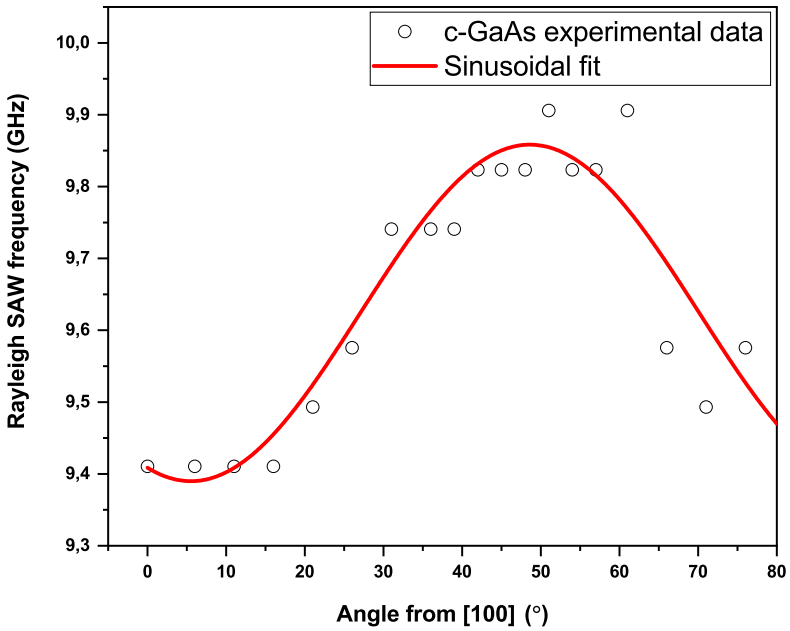


Figure 4.9: The dispersion curve of the Rayleigh SAW mode of c-GaAs which was used to identify the [100] and [110] propagation directions.

Table 4.3: The measured frequencies in the [100] and [110] direction and their corresponding velocities extracted from the dispersion curve of c-GaAs.

Wave Mode, direction	$\Delta F_{measured}(GHz)$	$V_{measured}(m/s)$
Rayleigh SAW [100]	9.41	2699.80
Rayleigh SAW [110]	9.82	2818.21
T [100]	10.24	2936.64
T [110]	10.73	3078.72
L [100]	18.16	5210.14
L [110]	18.82	5399.53

The results obtained were then used as starting parameter for the least square fitting method,

$$\chi^2(C_{11}, C_{12}, C_{44}) = \sum_{RSAW_i} (v_i^m - v_i^c)^2 + \sum_{L_i} (v_i^m - v_i^c)^2, \tag{4.4}$$

where v_i^m is the measured velocity and v_i^c is the calculated velocity and they yield the minimization of χ^2. The lowest χ^2 produces the elastic constants of the film. The starting parameters are $C_{11} = 130.6$, $C_{12} = 60.5$ and $C_{44} = 65.4$ GPa and the density used was $\rho = 5.37$ g/cm^3. The minimization method produced the elastic constants of c-GaAs. Table 4.4 has the values for the elastic constants obtained from the c-GaAs SBS measurements, in addition, other values found using different methods are listed for comparison.

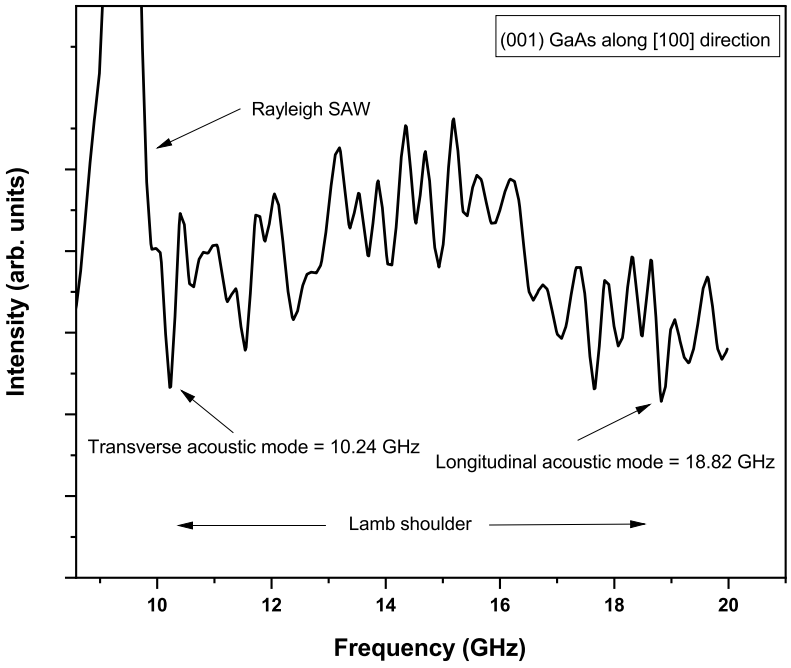


Figure 4.10: The Lamb shoulder region of the anti-Stokes side of SBS measurement taken in the [100] direction.

Table 4.4: The elastic constants of c-GaAs as obtained from various methods.

Constants	SBS	Neutron scattering[1]	Dipole model[81]	Shell Model[82]	LB[a 83]
C_{11}	126.7	120.0	119.0	120.0	118.0
C_{12}	60.5	57.6	57.0	57.0	53.5
C_{44}	56.7	58.0	60.0	60.0	59.4

[a] Landolt-Börnstein

The estimated elastic constants values are $C_{11} = 126.7$, $C_{12} = 60.5$ and $C_{44} = 56.7$ GPa. The C_{11} calculated here is 6.7 GPa higher than that determined through experimental neutron scattering[1]. However, the C_{12} and C_{44} are closer to the expected values as shown in Table 4.4. The difference in the values obtained for the elastic constants of c-GaAs with those in Table 4.4 are attributed to the uncertainty in the determination of the longitudinal and transverse acoustic wave positions in the acquired spectra. It is worth noting that taking longer measurements could help in reducing these uncertainties and will be done in the future.

4.4.2 Ion implanted GaAs

This section presents the results of the SBS measurements on Si^+ and Ar^+ implanted samples and a discussion of the major results. In contrast to the anisotropic GaAs, the distinguishing features that emerge upon ion implantation leading to the formation of *a*-GaAs are: a) a Sezawa wave peak, b) a Lamb shoulder with a thickness dependent minimum point and c) a Rayleigh SAW of lower frequency compared to that of *c*-GaAs. Figure 4.11 illustrates the SBS spectrum of *a*-GaAs in which the additional mode also known as the Sezawa wave (Sz) corresponds to a peak for a thin film layer on *c*-GaAs. The presence of the Sezawa peak is ascribed to the transverse acoustic velocity of the layer being less than that of the substrate. In addition, the decrease in Rayleigh SAW frequency signifies a softening in the layer after ion implantation. This is best described by the decrease in elastic constants of the amorphous samples compared to those of the *c*-GaAs.

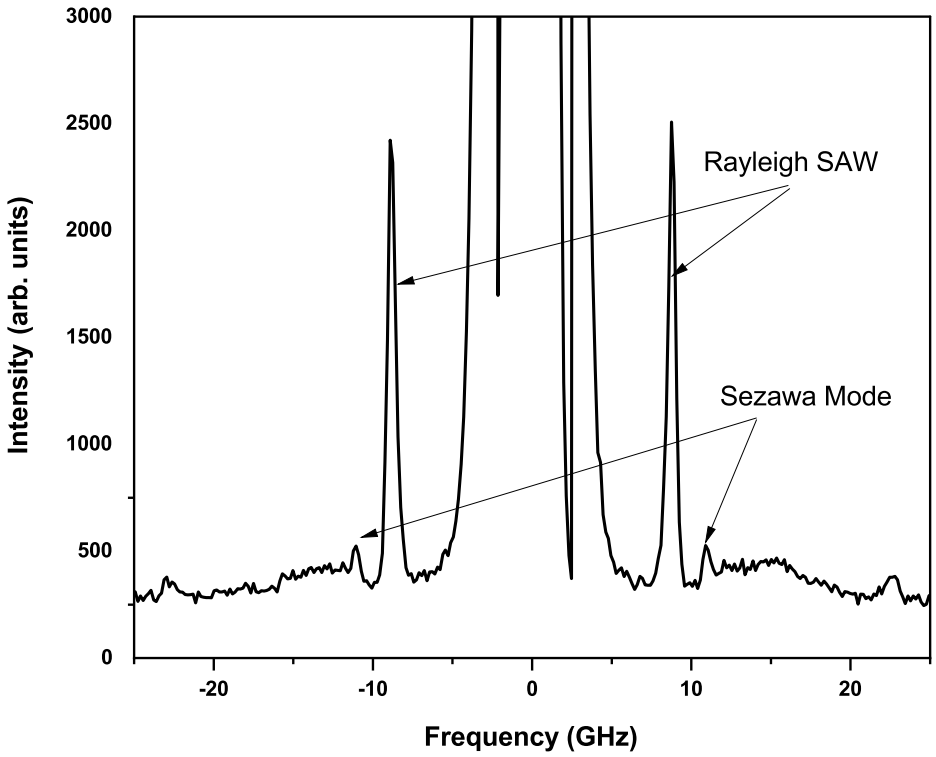


Figure 4.11: An SBS spectrum of *a*-GaAs.

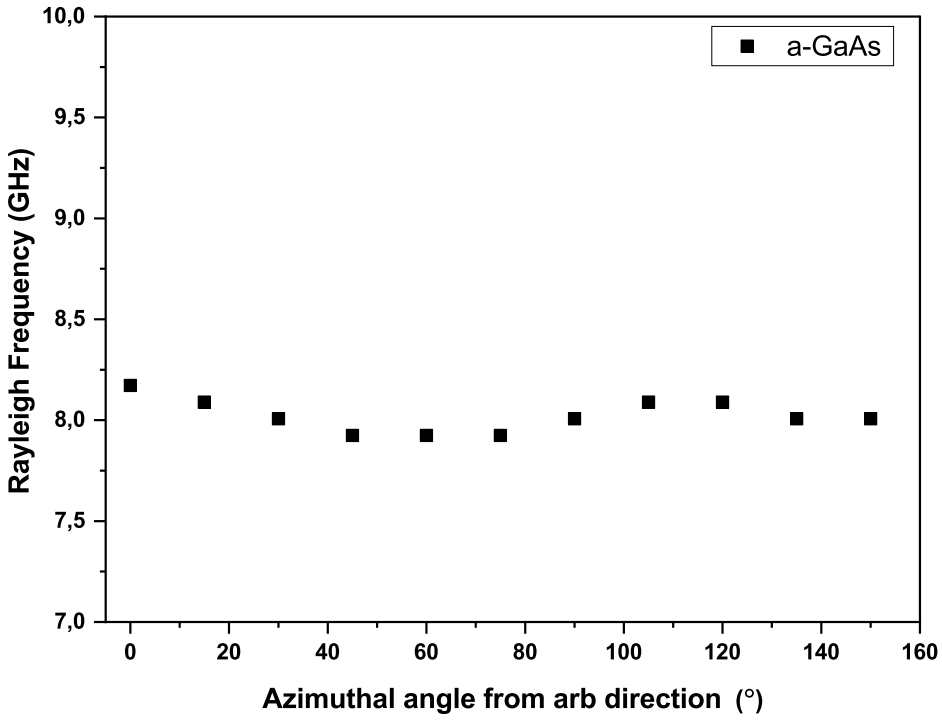


Figure 4.12: The dispersion curve of a-GaAs showing its isotropic surface.

While c-GaAs possesses an anisotropic surface in which the acoustic modes exhibit a sinusoidal azimuthal dispersion, a-GaAs is isotropic as indicated by the invariability of the Rayleigh wave in the azimuthal dispersion in Figure 4.12. Here SBS measurements were also taken at different azimuthal angles to obtain the relevant Rayleigh SAW frequencies. Figure 4.12 confirms the isotropy of the implanted surface of a-GaAs for a sample implanted with Ar^+ ions of energy 150 keV and dose 1×10^{16} ions/cm^2.

Argon implanted GaAs

The spectra from the set of samples bombarded with Ar^+ ions with energy 100 keV and doses ranging from 1×10^{14} to 5×10^{16} ions/cm^2 are shown in Figure 4.13. The spectrum of the sample implanted with the lowest dose shows it had not completely amorphized. This is seen with the absence of the Sezawa wave peak. From the Raman spectroscopy measurements in section 4.1 and Figure 4.2, it was observed that the sample implanted with 1×10^{14} ions/cm^2 has the amorphous phase mixed with the crystalline. This may explain its similarity to the un-implanted GaAs. The SBS spectra in the figure shows that the rest of the samples had decreasing Rayleigh SAW frequencies signifying a softening in the implanted layer. Additionally, these spectra all had the Sezawa wave peak. This can be attributed to the samples having a layered structure such that the surface had reached full amorphization. Furthermore, the 5×10^{16} ions/cm^2 implant, although amorphous,

recorded a Rayleigh SAW frequency of 8.79 GHz, a value greater than those of samples 5×10^{14} - 1×10^{16} ions/cm^2, which are in the range 8.59 - 8.09 GHz. The Raman spectroscopy measurements suggested the occurrence of partial re-crystallization within the damaged layer. This could mean the sample has regions of nanocrystals and amorphous phases.

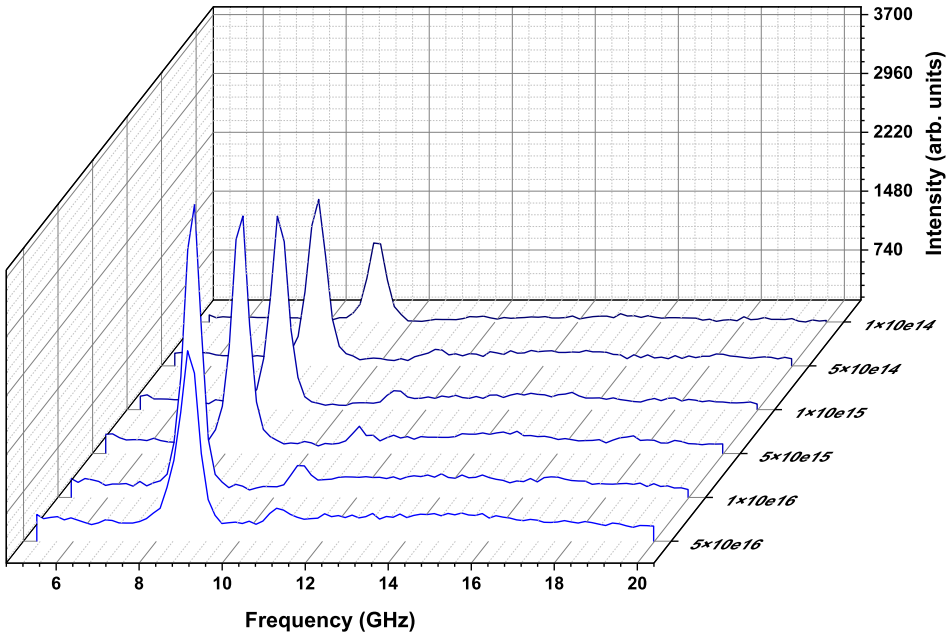


Figure 4.13: A series of SBS spectra of a-GaAs after argon ion implantation at varying doses measured at an incident angle of $\theta = 70°$.

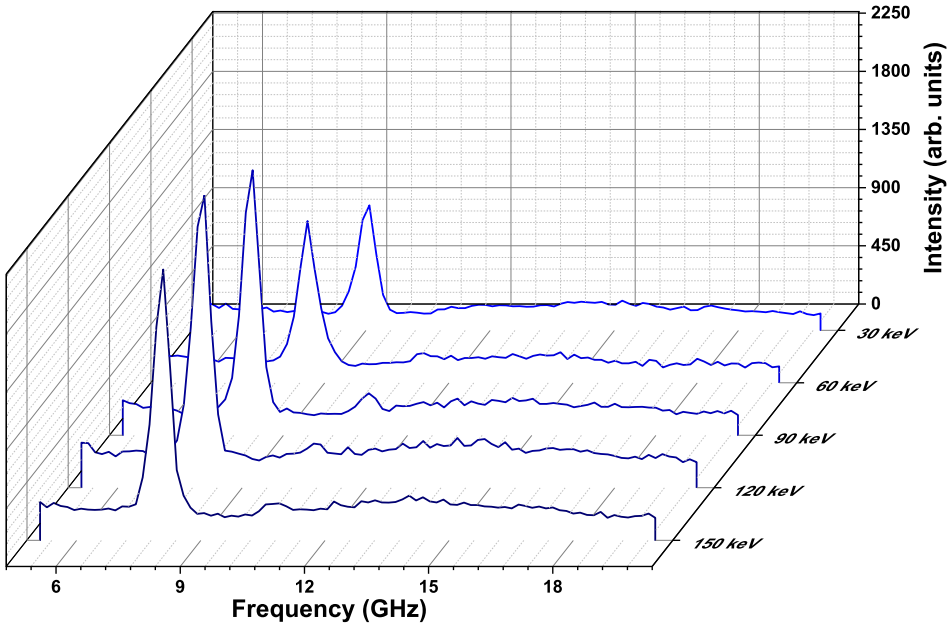


Figure 4.14: The SBS spectra of a-GaAs after argon ion implantation at different energies measured at an incident angle of $\theta = 70°$.

Figure 4.14 gives the spectra pertaining to the results of the samples implanted with a dose of 1×10^{16} ions/cm^2 and energies 30 to 150 keV. The Raman spectroscopy measurements taken for this group of samples confirmed the presence of an amorphous layer on the (001) GaAs substrate. On the other hand, in Figure 4.14, one spectrum for the measurement on the 30 keV sample exhibits the Rayleigh SAW peak at 9.08 GHz together with a Lamb shoulder. This frequency differs from that of crystalline GaAs, which are in the range 9.33 - 9.99 GHz obtained in the azimuthal dispersion curve. The SRIM thickness of the damage layer by irradiating (001) GaAs with 30 keV energy has been calculated to 60 nm. This relatively small thickness corresponds to a $k_{||}d$ of 0.67 with a Rayleigh SAW phase velocity of 2593.76 m/s. Comparing this value with the transverse velocity of the (001) GaAs substrate, which is 3078.72 m/s, limits the propagation of the Sezawa wave. This confirms the Raman measurement on the same sample in Figure 4.2b where a mixture of the amorphous phase with the crystalline one exists.

Figure 4.14 also shows the samples bombarded with energies 60 to 150 keV with a dose of 1×10^{16} ions/cm^2 had Rayleigh SAW and Sezawa wave peaks representing complete amorphization being achieved. The Rayleigh saw frequency decreases from 8.59 to 8.09 GHz while the Sezawa peak position changed from 11.39 to 10.73 GHz.

Silicon implanted GaAs

Another set of samples were implanted to create disordered GaAs on top of a crystalline substrate. These samples were implanted with Si^+ ions with energy 100 keV for doses ranging from 1×10^{14} to 5×10^{16} ions/cm^2. In the SBS measurements seen in Figure 4.15, the 1×10^{14} to 1×10^{15} ions/cm^2 samples had Rayleigh SAW frequencies in the 9.41 - 9.58 GHz range which falls in that of the *c*-GaAs azimuthal dispersion curve frequencies. Additionally, no Sezawa wave peaks were observed. This signifies that implantation of these samples did not create substantial damage to produce an amorphous layer. Further, the Raman spectroscopy measurements on these samples suggested incomplete amorphization where there was a mixture of damaged and undamaged regions.

In the measurements for the implantation's with 5×10^{15} to 5×10^{16} ions/cm^2 Sezawa wave peaks with frequencies 11.23 to 10.73 GHz were observed. Moreover, the Rayleigh SAW frequencies of these samples were in the range 8.91 to 8.25 GHz which are lower than those obtained for (001) GaAs thus indicating a softer layer. The Raman spectroscopy measurements were consistent with these results where all the spectra exhibited complete amorphization. This translates to lower elastic constants for implanted GaAs. Figure 4.15 shows the spectra of this set of samples.

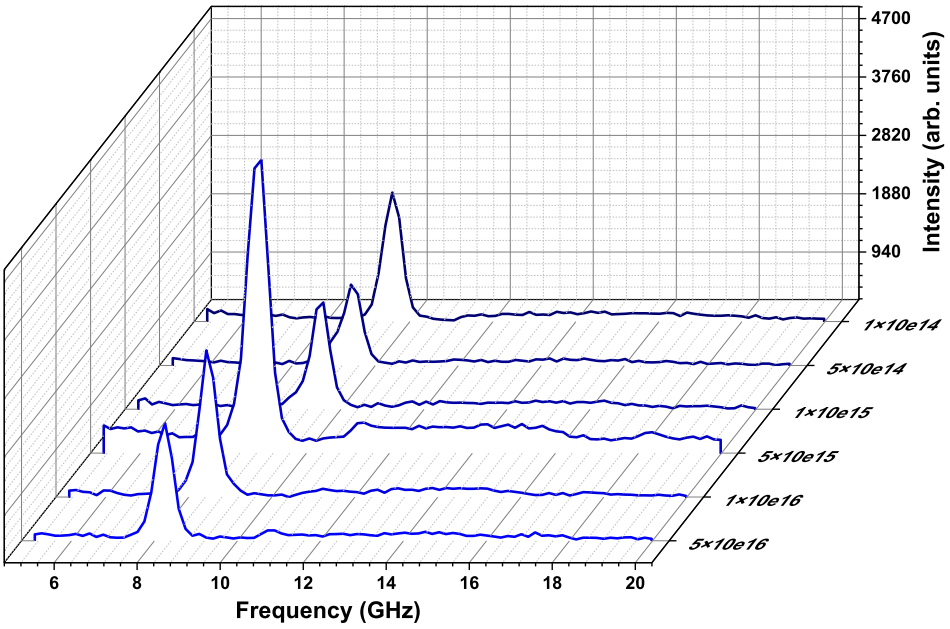


Figure 4.15: The anti-Stokes SBS spectra of a-GaAs after silicon ion implantation with different doses measured at an incident angle of $\theta = 70°$.

The spectra in Figure 4.16 pertain to implantation with a dose of $1{\times}10^{16}$ ions/cm^2 and energies varied from 30 to 150 keV. The spectra of the two lowest implants (30 and 60 keV) recorded no Sezawa wave peaks. However, the Rayleigh SAW frequencies of these two samples was less than that of crystalline GaAs, 9.08 and 8.75 GHz respectively. Moreover, the Raman spectroscopy measurements of these samples suggested complete amorphization had occurred. The SRIM thicknesses for these samples was 75 and 137.5 nm for the 30 and 60 keV samples, in that order, yielding $k_{||}d$ values of 0.83 and 1.53. The corresponding phase velocities were 2593.76 and 2500.29 m/s, respectively, limiting the propagation of the Sezawa wave. The 150 keV implanted sample did not have a Sezawa mode as well, however, unlike the aforementioned two, this one showed similar characteristics to the un-implanted. Here, the absence of the Sezawa wave mode can be attributed to lack of elasticity contrast and how thin the amorphous layer is due to re-crystallization. The Rayleigh SAW had a frequency of 9.41 GHz which falls in the range of that of the un-implanted GaAs, 9.33 - 9.99 GHz as obtained in the azimuthal dispersion curve. Further, the measured density ($\rho = 5.314$ g/cm^3) was in close proximity to that of c-GaAs obtained from XRD, $\rho = 5.319$ g/cm^3. Additionally, the Raman spectrum of this sample also showed it was not completely disordered.

The 90 and 120 keV implantations both produced Rayleigh SAW frequencies of 8.42 and 8.25 GHz, respectively. They also have 11.23 and 10.90 GHz corresponding to their Sezawa mode peaks, in that order. Further, the Raman spectroscopy measurements on these samples were in agreement.

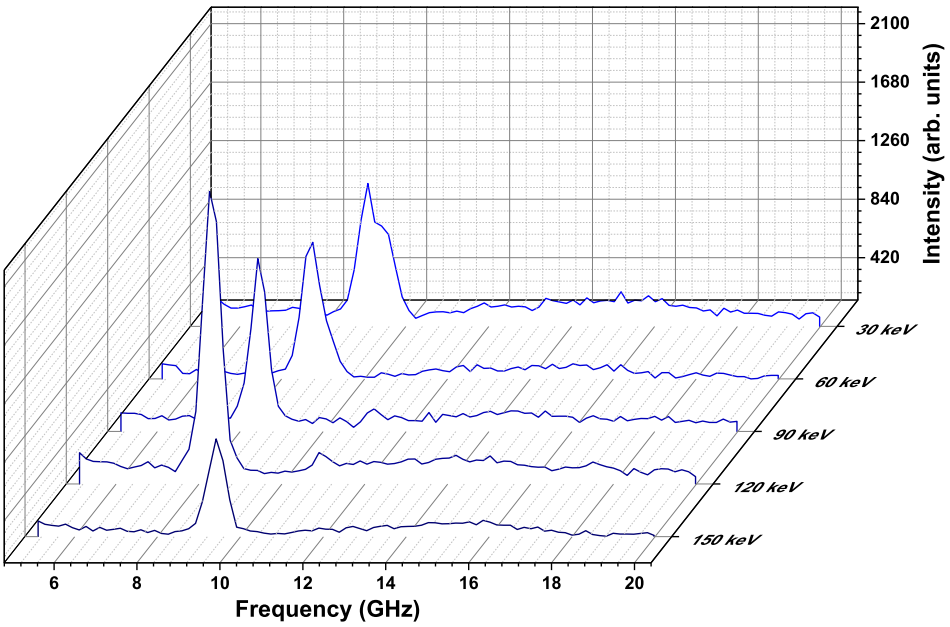


Figure 4.16: The anti-Stokes SBS spectra of a-GaAs following silicon ion implantation with varying energies measured at an incident angle of $\theta = 70°$.

4.4.3 Determination of elastic constant for ion implanted GaAs

The SBS spectra in the previous sub-sections provided the velocity which was used to plot the dispersion curves. The dispersion is obtained from the plot $k_{||}d$ against the phase velocities of acoustic phonons measured in the backscattering geometry. The dimensionless parameter, $k_{||}d$ was obtained from the product corresponding values of the $k_{||}$ (measured at incident angles in the range $\theta = 40$ - $80°$) and varied thicknesses. Furthermore, in ion implantation, the energy contributes to the depth of the damaged layer while the dose is responsible for the degree of disorder[84]. Consequently, the dose used (1×10^{16} ions/cm^2) was sufficient to create an amorphous layer, while the different ion energies were used to extend the $k_{||}d$ range by forming amorphous layers with thickness distributions suitable for extraction of the elastic constants. The thicknesses of the implanted layers used were those from the SRIM simulations which yield 60 to 225 nm for the argon ions and 75 to 287.5 nm for that of the silicon. Using equations,

$$C_{11} = \rho V_L^2, \tag{4.5}$$

$$\rho V_{RSAW}^2 - (\frac{C_{11}}{C_{44}} \times \frac{C_{44} - \rho V_{RSAW}^2}{C_{11} - \rho V_{RSAW}^2})^{1/2} \times (C_{11} - \frac{C_{12}^2}{C_{11}} - \rho V_{RSAW}^2) = 0, \tag{4.6}$$

the starting parameters intended for the fitting were obtained for the curves in Figures 4.17 and 4.18.

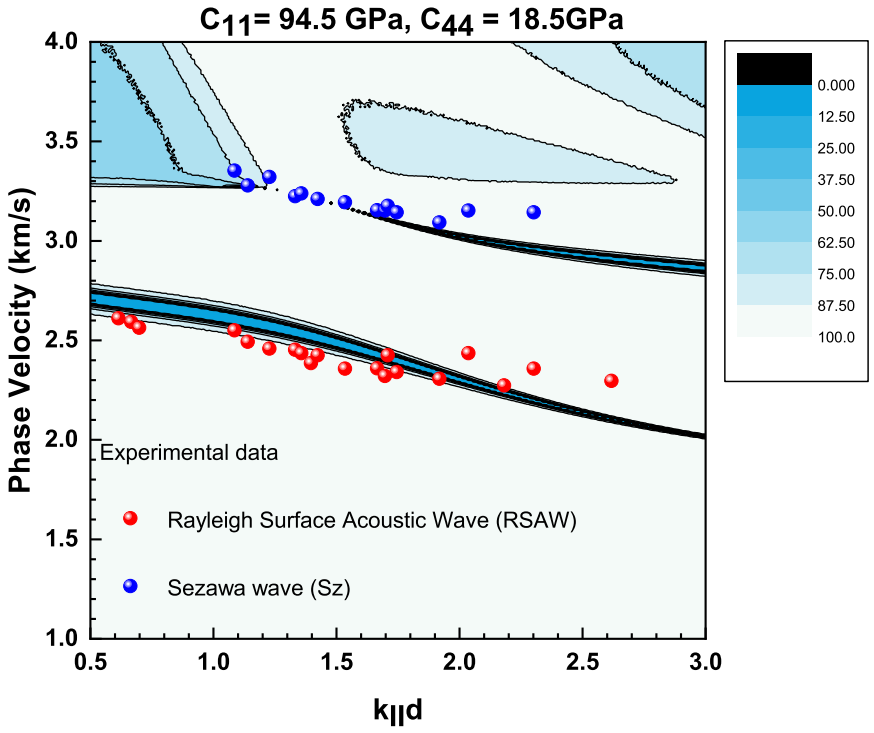


Figure 4.17: The velocity dispersion curve of the a-GaAs samples that were implanted with argon ions of energies from 30 – 150 keV.

The dispersion curve for a-GaAs formed by implanting argon ions with energies between 30 and 150 keV at a constant dose of 1×10^{16} ions/cm^2 is presented in Figure 4.17. SRIM simulations of the resulting amorphous layer revealed film thicknesses in the range of 60 - 225 nm. The presence of acoustic softening (within 8% of the estimated thickness range), guided modes propagating in the layer as well as the results of the Raman spectroscopy further indicate amorphization in all the samples. The SBS spectra in Figure 4.14 shows the 30 keV implantation (with a thickness of 60 nm) had a Lamb shoulder similar to the spectrum of c-GaAs. This could have been due to the dynamics of acoustic scattering in a thin amorphous layer embedded on the anisotropic (001) GaAs substrate such that the corresponding Rayleigh SAW of the layer occurs within the transonic region ($k_{||}d$), close to the transverse velocity of the substrate. This prohibits the propagation of the Sezawa waves within the amorphous layer.

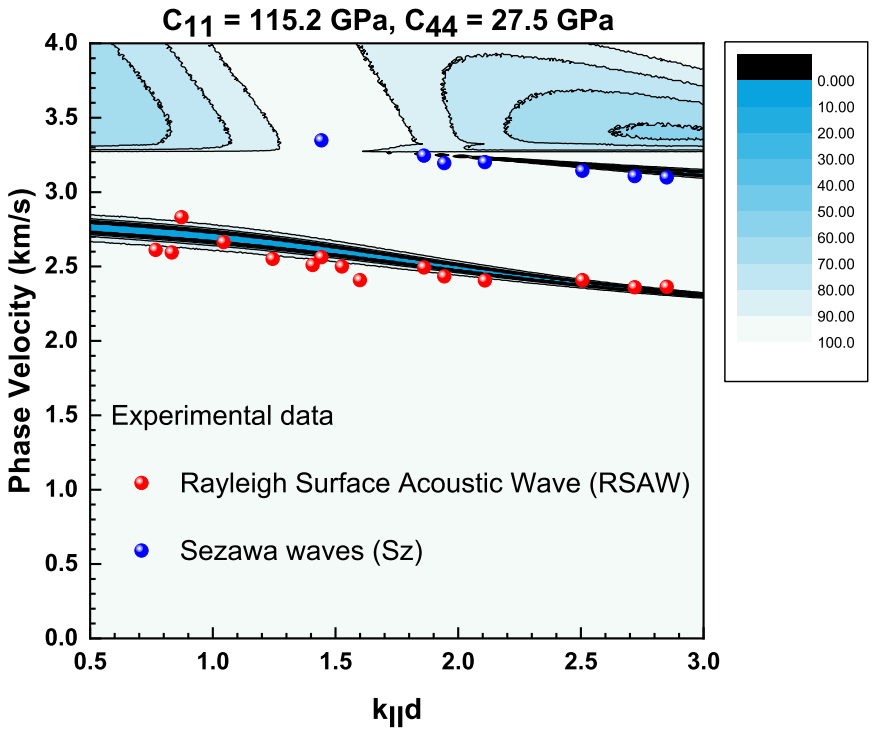


Figure 4.18: The velocity dispersion curve for the a-GaAs samples that were implanted with silicon ions of energies from 30 – 150 keV.

The samples implanted with silicon ions of energies from 30 - 150 keV at a dose of 1×10^{16} ions/cm^2 have a dispersion curve presented in Figure 4.18. The thickness values used in the dispersion relation have been determined using SRIM simulations in the range 75 - 287.5 nm. The velocity dispersion curve of the samples implanted with energy 30 and 60 keV, in Figure 4.16 differs from the other curves. This disparity is attributed to the variations in mass density.

The elastic constants of a-GaAs resulting from implantations of (001)GaAs with $^{30}Si^{+}$ ions of varying energy have been determined to C_{11} = 115.2 GPa and C_{44} = 27.5 GPa for an average density of 5.28 g/cm^3. These values are larger than those of the amorphous layer formed from $^{40}Ar^{+}$ on (001) GaAs which have been determined to be C_{11} = 94.5 GPa and C_{44} = 18.5 GPa for a density of 5.1 g/cm^3. The deviations between the raw data and the simulation are attributed to the inhomogeneity in the density values of the amorphous layers formed by implantation with ions having varied energy. Additionally, the contributions due to the amorphous layer thickness for the energies of the ions used cannot be ruled out. It is plausible that re-crystallization could lead to a reduction in layer thickness.

After the curves were fitted with simulated versions, the elastic constants were extracted. These

constants were then optimized using the least-square minimization,

$$\chi^2(C_{11}, C_{44}) = \sum_{RSAW_i} (v_i^m - v_i^c)^2 + \sum_{Sz_i} (v_i^m - v_i^c)^2, \tag{4.7}$$

where the lowest value of χ^2 produces the elastic constants of the film used to calculate velocity v_i^c. Plus, the calculated velocity was determined with,

$$V_i(C_{11}, C_{44}) = V_i^0 + \frac{\partial V_i^0}{\partial C_{11}}(C_{11} - C_{11}^0) + \frac{\partial V_i^0}{\partial C_{44}}(C_{44} - C_{44}^0), \tag{4.8}$$

using Mathematica. The coefficients $\partial V_i^0/\partial C_i$ are calculated for each point in the dispersion curve and V_i^0 is an experimental value. Every et al.[85] derived this method for anisotropic materials (single crystalline solids). Here the least square minimization method had to be adapted to optimize the C_{11} and C_{44} elastic constants and find their uncertainties using the velocities of the Rayleigh SAW and Sezawa waves[16,85].

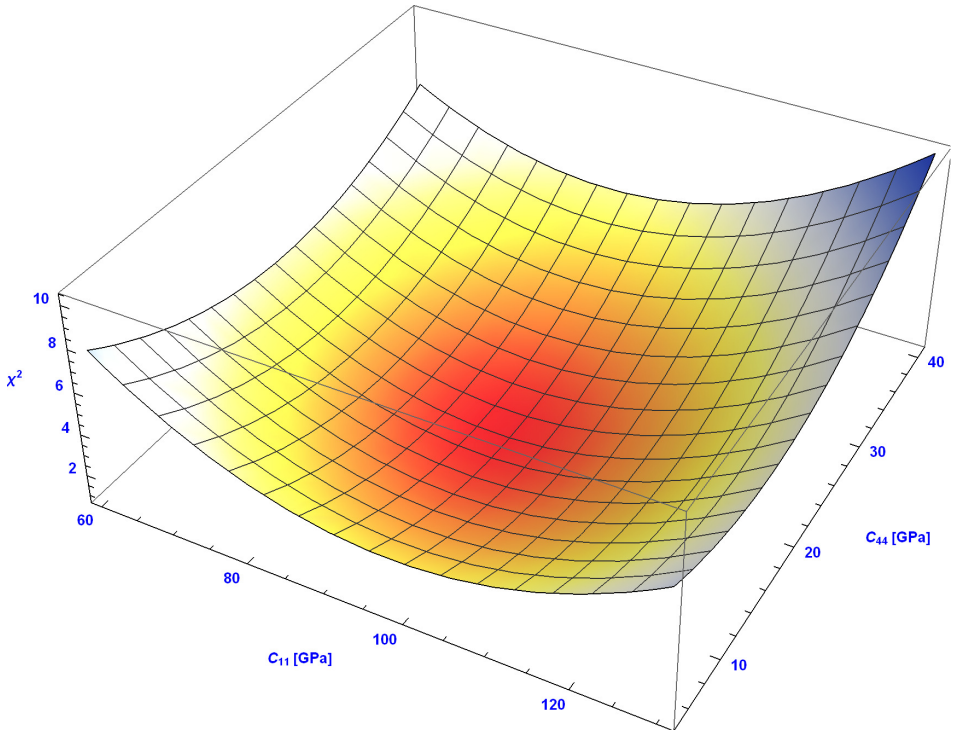


Figure 4.19: The contour plot of a-GaAs formed from implantation with Ar^+ obtained after an optimized minimization of χ^2 to find the elastic constants and their uncertainties.

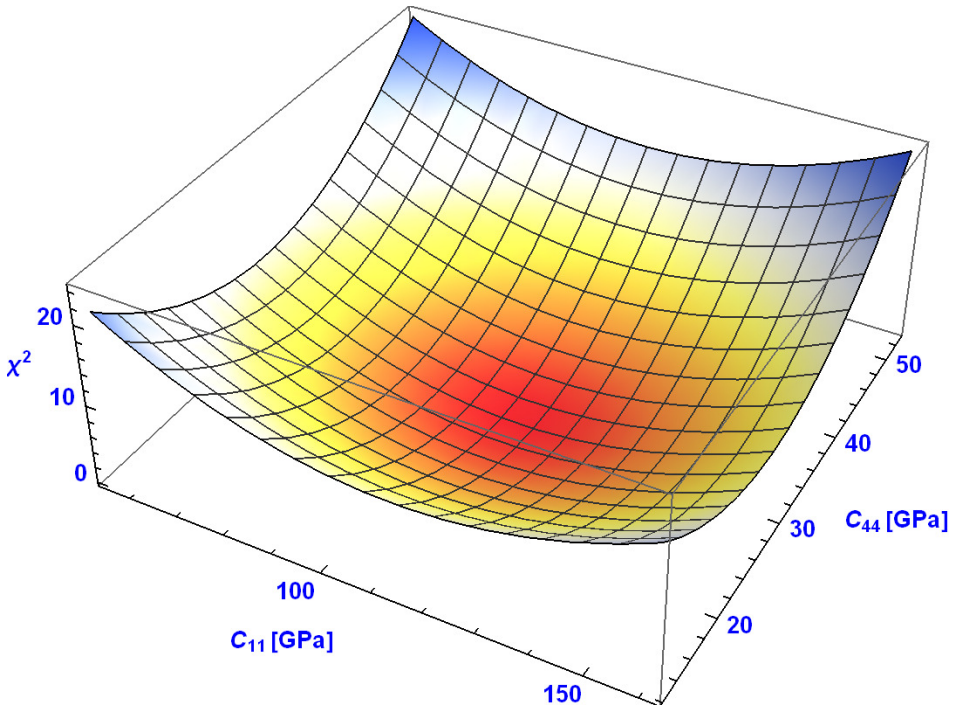


Figure 4.20: The contour plot of a-GaAs formed from implantation with Si^+ obtained after an optimized minimization of χ^2 to find the elastic constants and their uncertainties.

The two components of elastic constant tensor (C_{11}, C_{44}) for the isotropic a-GaAs formed by Ar^+ and Si^+ implantation have been determined using the surface elastodynamics Green's function to C_{11} = 94.5 and 115.2 GPa and C_{44} = 18.5 and 27.5 GPa, respectively. The optimized values of the elastic constants for samples implanted with Ar^+: Si^+ ions, respectively, have been determined to C_{11} = 95.8 GPa and C_{44} = 21.4 GPa: C_{11} = 111.8 GPa and C_{44} = 31.0 GPa. These values correspond to uncertainties of $\Delta C_{11} = \pm$ 1.5 GPa and $\Delta C_{44} = \pm$ 3.1 GPa: $\Delta C_{11} = \pm$ 3.4 GPa and $\Delta C_{44} = \pm$ 4.5 GPa for Ar^+ and Si^+ ion implanted GaAs, respectively. The uncertainties are calculated using the variance-covariance matrix as described by Ref[16]. The matrix produces the elliptical contour plots seen in Figures 4.19 and 4.20 where the variance determines the error in the elastic constant while the covariance is responsible for tilting the principal axes of the ellipse with reference to the elastic constant thus producing the most accurate values.

Ion implantation created heterostructures on the surfaces of the samples, this is evident with the results found above, specifically the density. This parameter showed most inhomogeneities were from argon implanted samples. As a result, the calculated standard deviation for Ar^+ and Si^+, respectively, are 0.39 and 0.03 g/cm^3. The larger value for Ar^+ led to a larger sum of squares and the χ^2 of 0.55 was obtained. On the other hand, the samples implanted with Si^+ had re-crystallization occurring at the surface while the amorphous layer was buried underneath. This led to a χ^2 minimization of 0.48. Another source of uncertainty in determining these results can

be greatly attributed to the experiment. In the course of the experiment, the change in scattering angle often changed the measurement spot and unlike Raman spectroscopy, SBS does not have a microscope to guide the experiment. Furthermore, this is believed to be the first report of elastic constants for a-GaAs using SBS.

Line-focus beam (LFB) acoustic microscopy[86] has thus far been the only method with a record of the elastic constants of a-GaAs. It was stated there that the C_{11} and C_{44} constants saw a decrease - from its c-GaAs elastic constants counterpart - of 17% and 41%, respectively after implantation. The argon ion implanted samples saw a decrease of 24.4% and 67.4% for C_{11} and C_{44}, respectively and a 11.8% and 45.3% decrease for C_{11} and C_{44}, for the silicon ion implanted samples. The differences seen here can be attributed to the amorphous state being a metastable one with several possible configurations and thus not unique. Structural relaxations could also lead to the changes in the amorphousness of the implanted layer.

Chapter 5

Summary and conclusion

The irradiation of GaAs with argon ($^{40}Ar^{+}$) and silicon ($^{30}Si^{+}$) ions using different doses and energies created an amorphous near-surface layer with different degrees of disorder and depth, respectively. The conditions of implantation that created these layered samples were doses of 1×10^{14} to 5×10^{16} ions/cm^2 at energy 100 keV and the energies from 30 to 150 keV at dose 1×10^{16} ions/cm^2 for both ions at room temperature. With SRIM the implantation process was simulated to estimate the thicknesses and they were found to have ranged from 60 to 225 nm and from 75 to 287.5 nm for argon and silicon ions, in that order.

An analysis was performed on *c*-GaAs with XRD to determine the orientation of the sample. This analysis provided proof that the *c*-GaAs had a dominant [400] lattice plane that is characteristic of the [100] structure of GaAs. The pattern also had a [200] lattice plane which had a weaker intensity compared to the former. This peak is a result of the multiplicity of the [100] planes. When Raman scattering measurements were conducted on the crystalline sample, the spectrum obtained had a TO phonon peak with a weaker intensity along with that of the LO phonon that obeyed the selection rules for the zinc-blende structure. With XRD and XRR the density of this crystalline material was determined, the values found were $\rho = 5.3194$ and 5.3714 g/cm^3, respectively. Both these values were close to that found in literature of $\rho = 5.3174$ g/cm^3. SBS measurements were performed on this sample as well, and the first step was to verify the anisotropic structure which also aids in determining the propagation directions. This action was vital in the calculation of the elastic constants. The values found for C_{11} and C_{44} were very close to those found in literature however, the C_{12} magnitude was higher.

The samples implanted with varying doses using argon ions were examined, and with the GIXRD patterns and Raman spectra obtained, the irradiation process was confirmed. The results of the

process proved that a poly-crystalline system that can be interpreted as short-range ordering by Raman spectroscopy and amorphous structure by SBS was created. Furthermore, the XRR densities provided more proof that the near-surface layer was different from the substrate. This was seen with the decrease in densities as the implantation dose increased. For this group of samples, the Raman spectroscopy results were in agreement with those of SBS, even for the highest dose implant which had spectra showing re-crystallization had occurred.

XRR analysis was one of the characterization techniques used for the samples implanted with varying energies of argon ions. Only two implants were analysed, and the outcome was $\rho = 4.787$ and 5.318 g/cm^3 for the samples implanted with the lowest and highest energies, respectively. On the other hand, using Raman spectroscopy on these samples revealed that amorphousness was achieved from the lowest energy implant. SBS agreed with this outcome. Although, with SBS the spectrum found had a Lamb shoulder and no Sezawa wave peak. Nevertheless, with this set, the elastic constants for *a*-GaAs were calculated for the first time using SBS. The result found was C_{11} = 95.8± 1.5 and C_{44} = 21.4 ± 3.1 GPa.

The samples implanted with different doses of silicon ions were analysed with GIXRD using the lowest, second highest and highest dose implants. The lowest and second highest dose implanted sample had multiple lattice planes while that of the highest only had one. This sample had a spectrum that was the opposite of the other two. It had an intense peak from the 2θ position where the others had a weak signal. In addition, where the other samples had intense signals the 5×10^{16} ions/cm^2 had weaker intensity peaks. The XRR densities obtained for this group were lower than that of *c*-GaAs (taken by XRR), with the highest dose implanted sample having the smallest value. Additionally, unlike the argon dose implanted set, the Raman spectroscopy and SBS spectra for this group were divided. Half the samples were polycrystalline while the other were completely amorphous. This means for silicon ions, a dose greater than 1×10^{15} ions/cm^2 is needed to bring about amorphousness.

The Raman spectroscopy measurements conducted for the set of samples implanted with silicon ions of different energies revealed samples implanted with energies 30 - 120 keV all showed amorphousness while that of 150 keV had symmetry peaks. The SBS spectra had a similar outcome. The frequency of the 150 keV sample was similar to that of the *c*-GaAs. Additionally, the SBS spectra for the 30 and 60 keV samples revealed that disorder was created however, it was not sufficient to have Sezawa waves observed in the measurements. This led to greater uncertainty in calculating the elastic constants. Nevertheless, the values of the constants found were C_{11} = 111.8 ± 3.4 and C_{44} = 31.0 ± 4.5 GPa.

The decrease in elastic constants of the *a*-GaAs found, with reference to *c*-GaAs, signifies that there was an amorphous surface created that was softer than its crystalline counterpart. Additionally, it signifies that the stoichiometry of GaAs was not destroyed by ion implantation. This decrease scheme also proves that ion mass contributes to the disorder created. Argon ions created greater damage compared to silicon ions under the same conditions.

The herein reported outcomes have laid a foundation for a study focusing on the exact conditions required for irradiating GaAs at room temperature (and other temperatures). This study could be able to explain why samples such as the ones implanted with argon ions highest dose and silicon ions highest energy had undergone re-crystallization when they had been expected to have the greatest disorder and damage depth, respectively. The study could also improve the uncertainty of the elastic constants of *a*-GaAs. Furthermore, the precise determination of the thickness of the amorphous layer remains a significant parameter in the determination of the elastic properties and also in confirmation of the SRIM simulations. HRTEM analysis is proposed in combination with RBS to determine the thickness of the disordered layer.

Additionally, it is not clear whether Ar^+ ion remain in the disordered GaAs or they diffuse out over time, this can be confirmed using surface sensitive technique such as XPS. The nature and configuration of the disordered layer is of great interest in the elaboration of the rigidity of the amorphous layer and subsequently in the in-depth interpretation of the elastic constants and their dependence on the Z of the ions used. We propose the use of multi wavelength Raman and XANES/EXAFS to determine the structural configuration of the various amorphous layers formed by ion implantation at various doses and energy. Lastly, using phonon confinement model the nature of the fractal formed during ion implantation and their dependence on the implantation conditions can be elucidated.

Bibliography

[1] K Jakata and A.G Every. Determination of the dispersive elastic constants of the cubic crystals Ge, Si, GaAs, and InSb. *Physical Review B*, 77(17):174301, 2008.

[2] A.G Every. *Dynamic methods for measuring the elastic properties of solids in Handbook of Elastic Properties of Solids, Liquids, and Gases. vol. 1.* Academic press, 2000.

[3] J.S Blakemore. Semiconducting and other major properties of gallium arsenide. *Journal of Applied Physics*, 53(10):R123–R181, 1982.

[4] D.S McGregor, R.A Rojeski, G.F Knoll, F.L Terry Jr, J East, and Y Eisen. Present status of undoped semi-insulating LEC bulk GaAs as a radiation spectrometer. *Nuclear Instruments and Methods in Physics Research Section A: Accelerators, Spectrometers, Detectors and Associated Equipment*, 343(2-3):527–538, 1994.

[5] G Hendorfer. Electron paramagnetic resonance experiments applied to SI-GaAs. *Progress in Crystal Growth and Characterization of Materials*, 35(1):99–114, 1997.

[6] D Ma, Y Chai, V Wang, E Li, and W Shi. Electronic structure, magnetic and optical properties of Cr-doped GaAs using hybrid density functional. *Computational Materials Science*, 113:75–79, 2016.

[7] M Bosi and C Pelosi. The potential of III-V semiconductors as terrestrial photovoltaic devices. *Progress in Photovoltaics: Research and Applications*, 15(1):51–68, 2007.

[8] K Jakata, D.M Wamwangi, C Sumanya, B.A Mathe, R.M Erasmus, S.R Naidoo, and J.D Comins. Thermally induced amorphous to crystalline transformation of argon ion bombarded GaAs studied with surface Brillouin and Raman scattering. *Nuclear Instruments and Methods in Physics Research Section B: Beam Interactions with Materials and Atoms*, 286:25–28, 2012.

[9] J.S Williams and M.W Austin. Low-temperature epitaxial regrowth of ion-implanted amorphous GaAs. *Applied Physics Letters*, 36(12):994–996, 1980.

[10] L Brillouin. Diffusion de la lumière et des rayons X par un corps transparent homogène. In *Annales de physique*, volume 9, pages 88–122, 1922.

[11] L.I Mandelstam. Light scattering by inhomogeneous media. *Zh. Russ. Fiz-Khim. Ova*, 58(381):146, 1926.

[12] J.R Sandercock. Trends in Brillouin scattering: Studies of opaque materials, supported films, and central modes. *Light Scattering in Solids III*, pages 173–206, 1982.

[13] W Pang. *Measurement of elastic properties of hard films using Brillouin scattering*. PhD thesis, 1998.

[14] A.G Every, W Pang, J.D Comins, and P.R Stoddart. Brillouin scattering study of guided modes in TiN films on high-speed steel. *Ultrasonics*, 36(1-5):223–227, 1998.

[15] W Pang, A.G Every, J.D Comins, P.R Stoddart, X Zhang, J.C Crowhurst, and D Pietersen. Brillouin scattering as a tool for characterizing surfaces, interfaces and thin films. In *Review of Progress in Quantitative Nondestructive Evaluation*, pages 1315–1322. Springer, 1998.

[16] J Kuria, D.M Wamwangi, J.D Comins, A.G Every, and D Billing. Surface Brillouin scattering study of tantalum nitride (TaN) thin films. *JOSA A*, 37(11):C125–C131, 2020.

[17] J Sapriel and J.C Michel. Brillouin scattering in microstructures involving GaAs. *Superlattices and Microstructures*, 1(4):353–355, 1985.

[18] R.P Sharma, R Bhadra, L.E Rehn, P.M Baldo, and M Grimsditch. Crystalline to amorphous transformation in GaAs during Kr ion bombardment: A study of elastic behavior. *Journal of Applied Physics*, 66(1):152–155, 1989.

[19] X Zhang, J.D Comins, A.G Every, P.R Stoddart, W Pang, and T.E Derry. Surface Brillouin scattering study of the surface excitations in amorphous silicon layers produced by ion bombardment. *Physical Review B*, 58(20):13677, 1998.

[20] U.V Desnica, I.D Desnica-Frankovic, M Ivanda, K Furic, and T.E Haynes. Morphology of the implantation-induced disorder in GaAs studied by Raman spectroscopy and ion channeling. *Physical Review B*, 55(24):16205, 1997.

[21] A Mohammed. *Theoretical studies of Raman scattering*. PhD thesis, KTH, 2011.

[22] C.S.R Rao, S Sundaram, RL Schmidt, and J Comas. Study of ion-implantation damage in GaAs: Be and InP: Be using Raman scattering. *Journal of Applied Physics*, 54(4):1808–1815, 1983.

[23] J Wang, H Mao, Z Zhu, Q Zhao, Z Li, and W Lu. Recrystallization behavior of high-fluence N^+-implanted GaAs studied by Raman spectroscopy. *Applied Surface Science*, 252(6):2186–2190, 2006.

[24] R Zallen. Optical studies of nanocrystalline GaAs: A review. *Journal of Non-crystalline Solids*, 141:227–232, 1992.

[25] S.K Mohanta, R.K Soni, N Gosvami, S Tripathy, and D Kanjilal. Morphological and micro-Raman investigations on Ar^+-ion irradiated nanostructured GaAs surface. *Applied Surface Science*, 253(10):4531–4536, 2007.

[26] I.D Desnica-Frankovic. Different recrystallization patterns of Si^+ implanted GaAs. *Journal of Applied physics*, 85(11):7587–7596, 1999.

[27] M Ivanda, S Music, M Gotic, A Turkovic, A.M Tonejc, and O Gamulin. The effects of crystal size on the Raman spectra of nanophase TiO2. *Journal of Molecular Structure*, 480:641–644, 1999.

[28] H Richter, Z.P Wang, and L Ley. The one phonon raman spectrum in microcrystalline silicon. *Solid State Communications*, 39(5):625–629, 1981.

[29] M.G Grimaldi, B.M Paine, M.A Nicolet, and D.K Sadana. Ion implantation and low-temperature epitaxial regrowth of GaAs. *Journal of Applied Physics*, 52(6):4038–4046, 1981.

[30] B.M Paine, N.N Hurvitz, and V.S Speriosu. Strain in GaAs by low-dose ion implantation. *Journal of Applied Physics*, 61(4):1335–1339, 1987.

[31] T.E Haynes and O.W Holland. Comparative study of implantation-induced damage in GaAs and Ge: Temperature and flux dependence. *Applied Physics Letters*, 59(4):452–454, 1991.

[32] F Nizzoli and J.R Sandercock. *Surface Brillouin scattering from phonons*. Elsevier Science Publishers B.V, 1990.

[33] M Beghi, A.G Every, V.B Prakapenka, P.V Zinin, et al. Measurement of the elastic properties of solids by Brillouin spectroscopy. 2012.

[34] Y Itin and F.W Hehl. The constitutive tensor of linear elasticity: its decompositions, Cauchy relations, null Lagrangians, and wave propagation. *Journal of Mathematical Physics*, 54(4):042903, 2013.

[35] G Li and J.R Gladden. High temperature resonant ultrasound spectroscopy: A review. *International Journal of Spectroscopy*, 2010, 2010.

[36] B.A Auld. *Acoustic fields and waves in solids*. John Wiley & Sons, 1973.

[37] M.J.P Musgrave. Crystal acoustics. holden-day, san francisco. *reprint: Acoustical Society of America, New York*, 1970.

[38] A.G Every, A.A Maznev, W Grill, M Pluta, J.D Comins, O.B Wright, O Matsuda, W Sachse, and J.P Wolfe. Bulk and surface acoustic wave phenomena in crystals: Observation and interpretation. *Wave Motion*, 50(8):1197–1217, 2013.

[39] X. Zhang. *Surface Brillouin scattering studies of bulk materials and thin layers*. PhD thesis, University of the Witwatersrand, 1999.

[40] G Güntherodt, S Blumenröder, B Hillebrands, R Mock, and E Zirngiebl. Light scattering in metallic compounds and thin supported layers. *Zeitschrift für Physik B Condensed Matter*, 60(423-432), 1985.

[41] M.G Beghi, A.G Every, P.V Zinin, and T Kundu. Brillouin scattering measurement of saw velocities for determining near-surface elastic properties. *Ultrasonic Nondestructive Evaluation. Kundu T (ed) CRC Press, Boca Raton*, pages 581–651, 2004.

[42] J.R Sanderocock. Light scattering from surface acoustic phonons in metals and semiconductors. *Solid State Communications*, 26(8):547–551, 1978.

[43] K.K Tiong, P.M Amirtharaj, F.H Pollak, and D.E Aspnes. Effects of As^+ ion implantation on the Raman spectra of GaAs:"Spatial correlation"interpretation. *Applied Physics Letters*, 44(1):122–124, 1984.

[44] G Dearnaley. Ion implantation. *Nature*, 256(5520):701–705, 1975.

[45] K Lee, M.S Ameen, L.M Rubin, D.D Roh, R Hong, R.N Reece, and D Yoon. Damage control of ion implantation for advanced doping process by using in-situ temperature control. *Materials Science in Semiconductor Processing*, 117:105164, 2020.

[46] M Ivanda, I Hartmann, and W Kiefer. Boson peak in the Raman spectra of amorphous gallium arsenide: Generalization to amorphous tetrahedral semiconductors. *Physical Review B*, 51(3):1567, 1995.

[47] C.W White, C.J McHargue, P.S Sklad, L.A Boatner, and G.C Farlow. Ion implantation and annealing of crystalline oxides. *Materials Science Reports*, 4(2):41–146, 1989.

[48] J.S Williams. Materials modification with ion beams. *Reports on Progress in Physics*, 49(5):491, 1986.

[49] A Carnera, A Gasparotto, M Berti, and R Fabbri. Influence of channeling effects on ion distribution and damage profiles during high energy ion implantation in Si. *Microchimica Acta*, 114(1):205–211, 1994.

[50] Semiconductor Wafer Inc. http://www.semiwafer.com/. Accessed: 28-02-2022.

[51] J.F Ziegler, M.D Ziegler, and J.P Biersack. SRIM-The stopping and range of ions in matter (2010). *Nuclear Instruments and Methods in Physics Research Section B: Beam Interactions with Materials and Atoms*, 268(11-12):1818–1823, 2010.

[52] D Cialla-May, M Schmitt, and J Popp. Theoretical principles of Raman spectroscopy. *Physical Sciences Reviews*, 4(6), 2019.

[53] L.A Nafie. Theory of Raman scattering. *Practical Spectroscopy Series*, 28:1–10, 2001.

[54] P Colomban and A Slodczyk. Raman intensity: An important tool to study the structure and phase transitions of amorphous/crystalline materials. *Optical Materials*, 31(12):1759–1763, 2009.

[55] I.P Herman. *Optical diagnostics for thin film processing*. Elsevier, 1996.

[56] N Esser and J Geurts. Raman spectroscopy. In *Optical Characterization of Epitaxial Semiconductor Layers*, pages 129–202. Springer, 1996.

[57] D.E Aspnes and A.A Studna. Dielectric functions and optical parameters of Si, Ge, GaP, GaAs, GaSb, InP, InAs, and InSb from 1.5 to 6.0 eV. *Physical Review B*, 27(2):985, 1983.

[58] J Epp. X-ray diffraction (XRD) techniques for materials characterization. In *Materials characterization using nondestructive evaluation (NDE) methods*, pages 81–124. Elsevier, 2016.

[59] B.D Cullity. *Elements of X-ray diffraction*. Addison-Wesley Publishing, 1956.

[60] Y Waseda, E Matsubara, and K Shinoda. *X-ray diffraction crystallography: Introduction, examples and solved problems*. Springer Science & Business Media, 2011.

[61] M Birkholz. *Thin film analysis by X-ray scattering*. John Wiley & Sons, 2006.

[62] O Sakata and M Nakamura. Grazing incidence X-ray diffraction. In *Surface Science Techniques*, pages 165–190. Springer, 2013.

[63] A Gibaud, M.S Chebil, and T Beuvier. X-ray reflectivity. In *Surface Science Techniques*, pages 191–216. Springer, 2013.

[64] M Yasaka. X-ray thin-film measurement techniques. *The Rigaku Journal*, 26(2):1–9, 2010.

[65] A Gibaud and S Hazra. X-ray reflectivity and diffuse scattering. *Current Science*, pages 1467–1477, 2000.

[66] U.V Desnica, I.D Desnica, M Ivanda, and T.E Haynes. Morphology of the implantation induced disorder in GaAs. *Nuclear Instruments and Methods in Physics Research Section B: Beam Interactions with Materials and Atoms*, 120(1-4):236–239, 1996.

[67] T Nakamura and T Katoda. Raman spectra from Si and Sn implanted GaAs. *Journal of Applied Physics*, 53(8):5870–5872, 1982.

[68] P Jayavel, R Kesavamoorthy, K Santhakumar, P Magudapathy, K.G.M Nair, and J Kumar. Raman scattering studies on low-energy nitrogen-implanted semi-insulating GaAs. *Nuclear Instruments and Methods in Physics Research Section B: Beam Interactions with Materials and Atoms*, 179(1):71–77, 2001.

[69] R Zallen, M Holtz, A.E Geissberger, R.A Sadler, W Paul, and M.L Thèye. Raman-scattering studies of implantation-amorphized gallium arsenide: Comparison to sputtered and evaporated a-GaAs films. *Journal of Non-Crystalline Solids*, 114:795–797, 1989.

[70] F.F Komarov. Self-annealing in ion-implanted Si and GaAs. *Vacuum*, 42(1-2):101–106, 1991.

[71] W Wesch, E Wendler, G Götz, and N.P Kekelidse. Defect production during ion implantation of various $A_{III}B_V$ semiconductors. *Journal of Applied Physics*, 65(2):519–526, 1989.

[72] T Nishino, T Matsumoto, and K Nakamae. Surface structure of isotactic polypropylene by X-ray diffraction. *Polymer Engineering & Science*, 40(2):336–343, 2000.

[73] M Bouroushian, T Kosanovic, et al. Characterization of thin films by low incidence X-ray diffraction. *Cryst. Struct. Theory Appl*, 1(3):35–39, 2012.

[74] V Jadhav, S.K Dubey, R.L Dubey, A.D Yadav, and D Kanjilal. Structural and optical studies of GaSb implanted with iron ions. *Surface and Coatings Technology*, 203(17-18):2670–2673, 2009.

[75] E Hüger, F Strauß, J Stahn, J Deubener, M Bruns, and H Schmidt. In-situ measurement of self-atom diffusion in solids using amorphous germanium as a model system. *Scientific Reports*, 8(1):1–8, 2018.

[76] J Stuke and G Zimmerer. Optical properties of amorphous III-V compounds. I. Experiment. *physica status solidi (b)*, 49(2):513–523, 1972.

[77] C Ascheron, A Schindler, R Flagmeyer, and G Otto. A comparative study of swelling, strain and radiation damage of high-energy proton-bombarded GaAs, GaP, InP, Si and Ge single crystals. *Nuclear Instruments and Methods in Physics Research Section B: Beam Interactions with Materials and Atoms*, 36(2):163–172, 1989.

[78] M.C Ridgway, C.J Glover, G.J Foran, and K.M Yu. Characterization of the local structure of amorphous GaAs produced by ion implantation. *Journal of Applied Physics*, 83(9):4610–4614, 1998.

[79] L.M Kotane. *Study of elastic properties of semiconductors by surface Billouin scattering.* PhD thesis, University of the Witwatersrand, 2010.

[80] Clemence Sumanya. *Surface brillouin scattering in opaque thin films and bulk materials.* PhD thesis, 2012.

[81] R Maranganti and P Sharma. A novel atomistic approach to determine strain-gradient elasticity constants: Tabulation and comparison for various metals, semiconductors, silica, polymers and the (ir)relevance for nanotechnologies. *Journal of the Mechanics and Physics of Solids*, 55(9):1823–1852, 2007.

[82] D.P DiVincenzo. Dispersive corrections to continuum elastic theory in cubic crystals. *Physical Review B*, 34(8):5450, 1986.

[83] A.G Every and A.K McCurdy. Second and Higher Order Elastic Constants, Landolt-Börnstein: Numerical Data and Functional Relationships in Sciences and Technology-New Series, vol. 29a, 2011.

[84] W.M Lau, I Bello, L.J Huang, X Feng, M Vos, and IV Mitchell. Argon incorporation in Si (100) by ion bombardment at 15-100 eV. *Journal of Applied Physics*, 74(12):7101–7106, 1993.

[85] A.G Every, C Sumanya, B.A Mathe, X Zhang, and J.D Comins. Optimized determination of elastic constants of crystals and their uncertainties from surface Brillouin scattering. *Ultrasonics*, 69:273–278, 2016.

[86] P Mutti, Z Sklar, G.A.D Briggs, and C Jeynes. Elastic properties of GaAs during amorphization by ion implantation. *Journal of Applied Physics*, 77(6):2388–2392, 1995.